DEPARTMENT OF PHYSICS
UNIVERSITY OF JYVÄSKYLÄ
RESEARCH REPORT NO. 11/2009

MASS MEASUREMENTS FOR EXPLOSIVE NUCLEOSYNTHESIS IN STARS

BY
VIKI-VEIKKO ELOMAA

Academic Dissertation
for the Degree of
Doctor of Philosophy

To be presented, by permission of the
Faculty of Mathematics and Natural Sciences
of the University of Jyväskylä,
for public examination in Auditorium FYS-1 of the
University of Jyväskylä on October 16, 2009
at 12 o'clock noon

Jyväskylä, Finland
October 2009

Preface

I am grateful for the supervisors Prof. Juha Äystö and Dr. Ari Jokinen for their guidance and, of course, for making it possible to do my PhD in the IGISOL group. Also, special thanks for realising this thesis go to the master trapper Dr. Tommi Eronen for teaching me how all the necessary bits really work, Dr. Christine Weber for helping many of my publications sound like physics and Dr. Saidur Rahaman for his technical assistance. Dr. Iain Moore along with his past and present minions are gratefully acknowledged on the help and fun with lasers. Iain has also been a true mentor on the mysteries of English language. So many people have helped me out with this thesis work, therefore, to keep the preface short all the rest IGISOL personnel are also acknowledged. Furthermore, I'd like to thank the workshop and other technical staff for their expertise and the secretariat for their help with the bureaucracy.

Large amount of recognition also goes to the Physics Department sports team Atomin Pamaus, which has provided the leisure activities in the form of running after a ball.

I want to thank my parents and siblings for their support and encouragement on my studies. And last, but not least, I thank my loving wife Hanna for her support and my first descendant Julia for keeping priorities in order and the second one for giving a convenient time frame for phd'ing.

This work has been supported by the EU's 6th Framework Programme "Integrating Infrastucture Initiative - Transnational Access", Contract Number: 506065 (EURONS, Joint Research Activities TRAPSPEC and DLEP) and by the Academy on Finland under the Finnish Centre of Excellence Programmes 2000-2005 (Projec No. 44875, Nuclear and Condensed Matter Physics Programme) and 2006-2011 (Nuclear and Accelerator Based Physics Programme at JYFL). Also financial support from the rector of the University of Jyväskylä and The Graduate School in Particle and Nuclear Physics (GRASPANP) is gratefully acknowledged.

Author Viki-Veikko Elomaa
Department of Physics
University of Jyväskylä
Finland

Supervisors Prof. Dr. Juha Äystö
Department of Physics
University of Jyväskylä
Finland

Dr. Ari Jokinen
Department of Physics
University of Jyväskylä
Finland

Reviewers Dr. Jerzy Szerypo
Faculty of Physics
University of Munich (LMU)
Garching, Germany

Prof. Dr. Thomas Nilsson
Fundamental Physics / Subatomic Physics
Chalmers University of Technology
Göteborg, Sweden

Opponent Prof. Dr. Kumar S. Sharma
Department of Physics and Astronomy
University of Manitoba
Winnipeg, Canada

Abstract

Elomaa, Viki-Veikko
Mass measurements for explosive nucleosynthesis in stars
Jyväskylä: University of Jyväskylä, 2009, x + 75 pp.
Department of Physics, University of Jyväskylä, Research Report 11/2009.
ISBN (paper copy) 978-951-39-3678-5
ISBN (pdf) 978-951-39-3679-2
ISSN 0075-465X

Atomic masses of almost 50 neutron-deficient isotopes in the region of tin and below were measured with the high-precision mass spectrometer JYFLTRAP Penning trap setup at the IGISOL facility in Jyväskylä. The masses have a direct impact on the nucleosynthesis modelling of neutron-deficient isotopes and were used for rp- and νp-process model calculations. For example, the abundance of stable molybdenum and ruthenium isotopes can not be explained with present knowledge. The rp process has been predicted to end in the SnSbTe-cycle. The new mass measurements do not allow a strong SnSbTe-cycle to be formed.

A carbon-cluster ion source based on laser ablation has been constructed. The source was used for investigating systematic effects of the JYFLTRAP setup. The mass-dependent effect and a residual uncertainty of the system were quantified. The obtained values were $\sigma_{\mathrm{m}}(r)/r = (7.8 \pm 0.3 \times 10^{-10}/u) \times \Delta m$ for mass dependence and $\sigma_{\mathrm{res}}(r)/r = 1.2 \times 10^{-8}$ for the residual uncertainty. If the mass difference range between the reference ion and ion of interest is restricted to $\pm$24, the values are $\sigma_{\mathrm{m,lim}}(r)/r = (7.5 \pm 0.4 \times 10^{-10}/u) \times \Delta m$ and $\sigma_{\mathrm{res,lim}}(r)/r = 7.9 \times 10^{-9}$, respectively.

The JYFLTRAP setup was used to survey the production of neutron-deficient nuclides with proton- and ^{3}He-induced fusion evaporation reactions. The measured proton-induced relative yields were compared to a statistical model calculation. The survey will help to plan future mass and spectroscopy measurements in the region.

List of Publications

This thesis work is based on the publications listed below. The author has performed data analysis in all publications and been the one responsible on the on-line measurements. Also, he has built, tested and used the carbon-cluster ion source for systematic studies of the JYFLTRAP setup. The author of this thesis is the main writer of publications III–VI and has helped writing I–III. The nucleosynthesis calculations in publication I were performed by C. Fröhlich and colleagues while in the publication III the calculations were performed by H. Schatz. The cross-section calculations in the publication IV were performed by V. Rubchenya.

I *Mass Measurements in the Vicinity of the rp-Process and the νp-Process Paths with the Penning Trap Facilities JYFLTRAP and SHIPTRAP*
C. Weber, V.-V. Elomaa, R. Ferrer, C. Fröhlich, D. Ackermann, J. Äystö, G. Audi, L. Batist, K. Blaum, M. Block, A. Chaudhuri, M. Dworschak, S. Eliseev, T. Eronen, U. Hager, J. Hakala, F. Herfurth, F. P. Heßberger, S. Hofmann, A. Jokinen, A. Kankainen, H.-J. Kluge, K. Langanke, A. Martín, G. Martínez-Pinedo, M. Mazzocco, I. D. Moore, J. B. Neumayr, Yu. N. Novikov, H. Penttilä, W. R. Plaß, A. V. Popov, S. Rahaman, T. Rauscher, C. Rauth, J. Rissanen, D. Rodríguez, A. Saastamoinen, C. Scheidenberger, L. Schweikhard, D. M. Seliverstov, T. Sonoda, F.-K. Thielemann, P. G. Thirolf, and G. K. Vorobjev
Phys. Rev. C **78**, 054310 (2008).

II *Mass Measurements and Implications for the Energy of the High-Spin Isomer in ^{94}Ag*
A. Kankainen, V.-V. Elomaa, L. Batist, S. Eliseev, T. Eronen, U. Hager, J. Hakala, A. Jokinen, I. D. Moore, Yu.N. Novikov, H. Penttilä A. Popov, S. Rahaman, S. Rinta-Antila, J. Rissanen, A. Saastamoinen, D. M. Seliverstov, T. Sonoda, G. Vorobjev, C. Weber, and J. Äystö
Phys. Rev. Lett. **101**, 142503 (2008).

III *Quenching of the SnSbTe Cycle in the rp Process*
V.-V. Elomaa, G. K. Vorobjev, A. Kankainen, L. Batist, S. Eliseev, T. Eronen, J. Hakala, A. Jokinen, I. D. Moore, Yu. N. Novikov, H. Penttilä, A. Popov, S. Rahaman, J. Rissanen, A. Saastamoinen, H. Schatz, D. M. Seliverstov, C. Weber, and J. Äystö
Phys. Rev. Lett. **102**, 252501 (2009).

IV *Light-Ion Induced Reactions in Mass Measurements of Neutron-Deficient Nuclides Close to* $A = 100$
V.-V. Elomaa, T. Eronen, U. Hager, J. Hakala, A. Jokinen, A. Kankainen, I. D. Moore, S. Rahaman, J. Rissanen, V. Rubchenya, C. Weber, and J. Äystö
Eur. Phys. J. A **40**, 1 (2009).

V *Development of a Carbon-Cluster Ion Source for JYFLTRAP*
V.-V. Elomaa, T. Eronen, U. Hager, A. Jokinen, T. Kessler, I.D. Moore, S. Rahaman, C. Weber, and J. Äystö
(EMIS2007 Conference Proceedings) Nucl. Instrum. Meth. Phys. Res. B **266**, 4425 (2008).

VI *Systematic studies of the Penning trap mass spectrometer JYFLTRAP*
V.-V. Elomaa, T. Eronen, J. Hakala, A. Jokinen, A. Kankainen, I.D. Moore, S. Rahaman, J. Rissanen, C. Weber, and J. Äystö
Nucl. Instrum. Meth. Phys. Res. A., Article in Press
doi:10.1016/j.nima.2009.09.002

Contents

List of Figures

1 Introduction

During the last few years the JYFLTRAP group has been very productive with their mass measurement program. In particular, the refractory elements have been an area of expertise due to the unique production capabilities of the ion guide technique. Much of the work has concentrated on fission fragments as, for example, in the PhD thesis work of U. Hager [1]. Another area of expertise is in the ultra precise Q-value measurement work as presented in the thesis of T. Eronen [2]. Some results have also been published on isotopes located on the neutron-deficient side of the valley of β stability, see for example [3]. The course of this work was to further enhance the knowledge on the isotopes on that side of the nuclear chart.

Much of the motivation for the mass measurement work at JYFLTRAP arises from stellar nucleosynthesis. The present knowledge on the origin of all matter lies in stellar processes, apart from that produced by primordial nucleosynthesis. As the famous astronomer and popularizer of natural sciences Carl Sagan has stated: "We are made of star stuff." But the question asked today is, how did that happen? Theoretical calculations try to answer this question. To do this properly, to test models, accurate experimental binding energies of nuclides are among the essential quantities needed. As long as systematic effects of the setup are known well enough, a Penning trap system can provide high precision mass data on rare isotopes.

Mass measurements are not the only programme that the JYFLTRAP system is used for. In addition, the setup can be used to provide isobarically – and sometimes even isomerically – clean beams for spectroscopy purposes. Another novel use is to study production yields. Because of different chemical properties between elements the measured yields are not direct production yields. Instead, relative isotopic yields can be determined with good accuracy and compared to those from reaction cross section calculations. The yield information can be used to plan future (mass) measurements at IGISOL.

2 Star stuff

2.1 Stellar nucleosynthesis

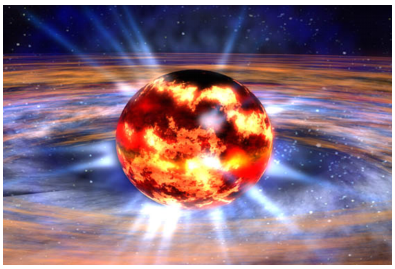

The origin of life and matter has always intrigued the human imagination. Although the question can be philosophical in nature there are some parts which science of today can help to unwrap. Life itself is considered to consist more of chemistry having a tinge of physics, whereas the origin of matter is mostly physics. Approaches in the studies for the production of the elements, the nucleosynthesis, are based on a combination of nuclear physics and astrophysics research which has given a birth to an active field called nuclear astrophysics.

The present knowledge on the nucleosynthesis is that it started in the Big Bang where the first protons and neutrons were formed from the quark-gluon plasma. During the first twenty minutes after the Bang the universe cooled down until the temperature was low enough to allow the protons and neutrons to fuse into deuterium. Only when deuterium was formed was it possible to get ^{4}He. This formation period did not last long before the temperature dropped low enough to allow nuclear fusion. The hydrogen to helium-4 mass fraction of about 75 to 25 seen today is believed to be mostly responsible from the primordial nucleosynthesis. A mass abundance of only 0.01% of deuterium was left behind after the helium formation and some trace amounts of lithium and beryllium. The following nucleosynthesis happens mostly in stars.

A star ignites when it has sufficient amount of compressed matter in a small enough region. The kinetic energy of atoms becomes high enough to create temperatures where the repulsive Coulomb energy is overcome and fusion starts. In stars having a mass limited to that of the Sun or smaller, but being massive enough to sustain fusion reactions, the nucleosynthesis is usually dominated by the pp-chain. It converts protons into helium first by fusing two protons to create deuterium in a temperature range of 10^6 K to 10^7 K. Deuterium then fuses with a proton resulting in ^{3}He. When two ^{3}He nuclides collide they can form ^{4}He and two protons. This is the main pp branch and is the most abundant channel of ^{4}He production in the pp-chain. The next most abundant branch is to fuse ^{3}He nuclides with an α particle to form ^{7}Be. Via electron capture, ^{7}Li is formed which then forms two ^{4}He nuclides after

a proton capture. It is also possible for the ^{7}Be nuclei to fuse with a proton into ^{8}B. This decays into ^{8}Be and further breaks again into two ^{4}He nuclides. Because ^{4}Li is not stable enough it is unlikely that ^{3}He would directly fuse with a proton.

The first stars formed right after the Big Bang were made of purely hydrogen and helium. Therefore, the next step in nucleosynthesis after the pp-chain is the triple-alpha process which can start when hydrogen has burned into helium. First, two helium nuclides fuse into ^{8}Be, which is unstable and decays back into its components. If the temperature is high enough however the beryllium is formed at a rate fast enough that it has time to fuse with a third ^{4}He into ^{12}C. The formation of ^{12}C is allowed by the fact that the carbon has an excited state which is in resonance with the energy of ^{4}He+^{8}Be, the energy state predicted by Fred Hoyle [4]. The hotter and denser the environment, the further up the nuclide chart the fusion of α particles and light nuclei can proceed. The element formation can proceed up to the iron region if the star mass is larger than 10 times the mass of the Sun.

Following the triple-alpha process another helium-producing process becomes possible. This is the so-called CNO cycle. If a star has some heavier elements inside, namely ^{12}C, it acts as a catalyst fusing four protons into ^{4}He via nitrogen and oxygen isotopes. The process needs higher temperatures than the pp-chain due to a higher Coulomb barrier. This process is dominant in stars that are heavier than about 1.5 times the mass of the Sun.

The energy and element production in the processes above can be understood by the fact that the mass of an atom consists also of the binding energy between the nucleons. Due to the energy release in fusion reactions, the production of elements up to iron can be explained fairly easily in steady burning processes in stars of different age and mass. The mass of the Sun is enough to sustain the nucleosynthesis until the region of the CNO-cycle. Production of the elements heavier than iron need somewhat more exotic hotter and denser sites than ordinary stars.

When the helium burning starts to take place the star expands into a red giant finally spewing the outer layers into space and the remnants form a white dwarf. Depending on the mass of the star the white dwarf can further collapse into a neutron star or even a black hole. The collapse happens explosively and is witnessed as a supernova. The Sun has enough mass to produce only the white dwarf. If the star mass is approximately eight times $M_{\odot}$ the core will have enough mass to overcome the Chandrasekhar limit of 1.4 solar masses. Then a neutron star can be formed.

It is possible for a white dwarf, which is initally below the Chandrasekhar limit, to produce a supernova explosion. For that it needs a companion star that feeds matter onto its surface until the limit is achieved. During the feeding the temperature in the surface of the dwarf star can increase so high that nucleosynthesis takes place.

In a neutron rich environment two different neutron-capture processes can take place and produce the isotopes heavier than iron on the neutron rich side of the valley of β stability. These are the s and r processes which are the slow and rapid neutron-capture processes,

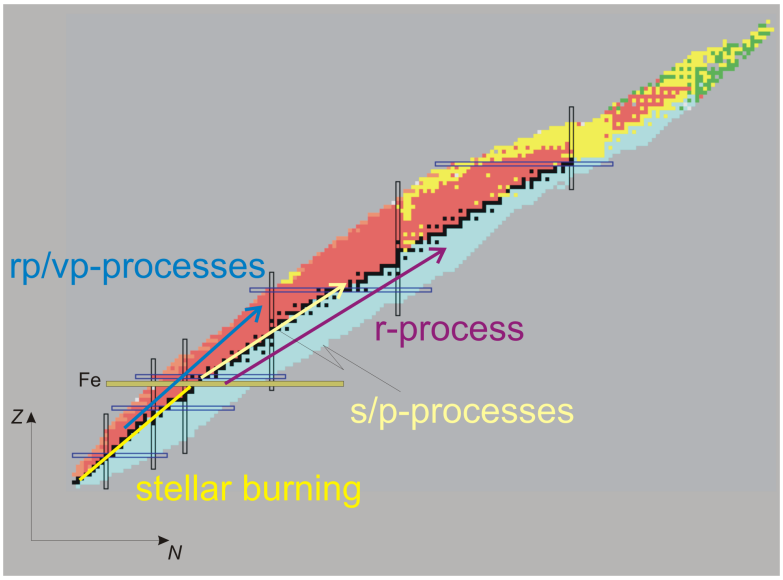

Fig. 2.1: Schematic view of different stellar nucleosynthesis paths.

respectively. The r process happens in core-collapsing supernovae and the s process mainly in the Asymptotic Giant Branch stars. However, these processes can not explain the abundance of certain stable isotopes, for example ^{92}Mo, on the neutron-deficient side of the Segré chart. To produce these isotopes different kinds of mechanisms are needed. The p process proceeds along the stable elements producing neutron-deficient nuclei via photodisintegration where an energetic photon penetrates into a nuclide and neutrons, protons or α particles are ejected. Another name for the p process is the γ process. The p process is thought to happen in core-collapse supernovae.

In order to understand the relatively high abundances of several neutron-deficient isotopes such as ^{92}Mo and ^{96}Ru other processes have to be investigated. Among them are the rapid-proton capture (rp) and neutrino-induced p process (νp). The present thesis concentrates on the investigation of these processes.

2.2 Rapid proton capture

The rapid proton-capture process (rp process) is a sequence of (p,γ) reactions and β^+ decays [5], which requires a hydrogen rich hot environment to happen. Possible sites for the rp

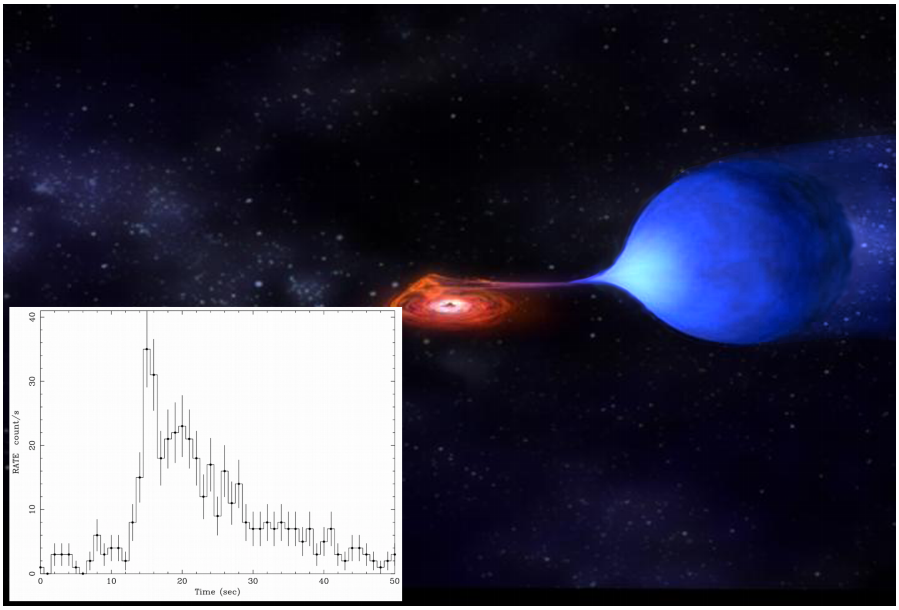

Fig. 2.2: An artist's (Credit:NASA) impression of a X-ray burster binary star system. A red giant (blue) feeds hydrogen rich material to the accretion disk (red) around a neutron star. Bottom left corner is a light curve, assigned as a type I X-ray burst, measured from the X-ray binary 4U 1708-40 with BeppoSAX in 1999 [7].

process are X-ray bursters. These are binary stellar objects where a small, but heavy object, for example a neutron star or a black hole, is accompanied by a light-element (hydrogen and/or helium) rich partner, often a red giant. Hydrogen and helium are fed into the accretion disk around the dense object typically over the order of hours to days before the material burns.

In a Type I X-ray burster the burning happens explosively in a thermonuclear runaway within 10-100 s and the observed X-ray light curve has a sharp rise following a slow decline. In Type II X-ray bursters the recurrence of the bursts is more frequent and the overall shape of the burst is different to Type I. Only a few Type II bursters are known whereas there are more than 80 Type I X-ray bursters catalogued [6].

Satellites have been sent to space to study the X-ray bursters and other X-ray emitting objects, including EXOSAT, BeppoSAX, RXTE and Chandra. Of these, EXOSAT was operational from 1983 to 1986, BeppoSAX was launched into orbit in 1996 and was operational until spring 2002. RXTE (Rossi X-ray Timing Explorer) has been in orbit since the end of

1995 and the Chandra satellite since 1999. Fig. 2.2 shows an artist's impression of a X-ray burster binary with a light curve measured with the BeppoSAX satellite.

The X-ray light flashes measured are used to determine the underlying physics of the binary systems. One feature that can be determined from the X-ray bursts' light curves is the distance to the binary star system. Since the rp process is sensitive to the hydrogen content related to the burst, if the rp process is known well enough the H content can be determined. Following this, L_{Edd} can be determined. The Eddington luminosity, L_{Edd}, is the luminosity where the outward radiation pressure overcomes the gravitational force. By comparing L_{Edd} to the apparent luminosity the distance to the binary system can be determined. [8]

At present the experimental equipment is not sensitive enough to monitor closely all the components of the star system, thus one has to rely on modelling the physics. For example, in Ref. [9] one-dimensional multi-zone calculations combined with the latest nuclear physics data are used to give a model for a sequence of X-ray bursts. In the same publication effects of varying some of the nuclear physics parameters are studied.

It may well be that the X-ray bursters don't contribute to the abundance of different isotopes heavier than iron, because there has been no mechanism found that could blow the material out from the neutron star system. Nevertheless, by studying the rp process and knowing the conditions where the rp process can happen, different stellar objects and the matter itself under extreme conditions can be studied more closely. Since the X-ray bursters happen repeatedly, they make an excellent, although remote, laboratory for the studies of material under extreme conditions.

Recently another process to explain the production of neutron-deficient isotopes has been proposed. This is called the νp process [10]. This process is thought to happen when strong neutrino fluxes create proton-rich ejecta in supernovae. Anti-neutrinos are absorbed by protons producing neutrons which are then captured by neutron-deficient nuclides. The process would contribute to the production of $A > 64$ nuclei. For example, the abundance of light molybdenum and ruthenium isotopes is hoped to be explained with this process, as is with the rp process.

2.3 Atomic masses in nucleosynthesis

For modelling stellar nuclear processes the atomic masses of the relevant isotopes are of key importance. One way to visualise the importance is in the Saha equation. In the rp process the equation describes the abundance ratio of (p,γ)–(γ,p) equilibrium in isotonic chains between the neighboring nuclei

$$\frac{Y_{n+1}}{Y_n} = \rho \frac{G_{n+1}}{2G_n} \left(\frac{A_{n+1}}{A_n} \frac{2\pi\hbar^2}{m_u kT} \right)^{3/2} exp\left(\frac{S_{n+1}}{kT} \right). \tag{2.1}$$

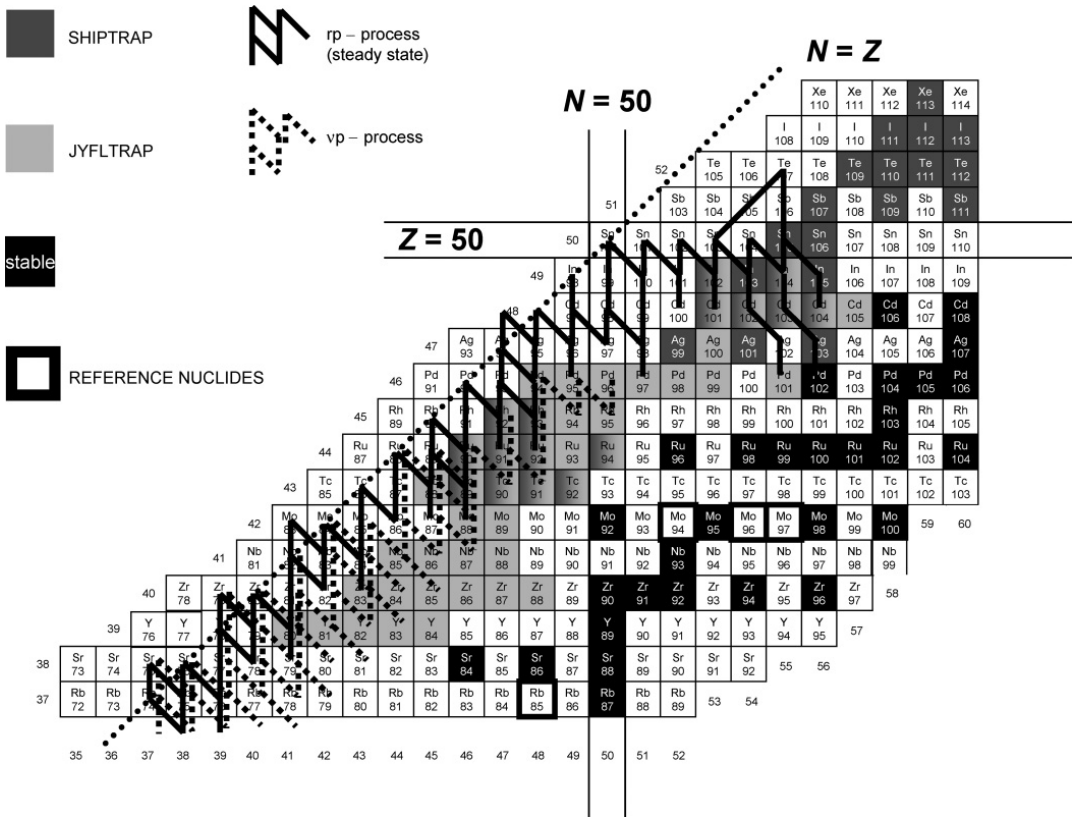

Fig. 2.3: Rp- and νp-process paths below ^{100}Sn [11].

Here Y_{n+1} and Y_n are the abundances of an initial and final nucleus of a single proton capture reaction, T is the temperature, ρ the proton number density, G the partition function, A the mass number, m_u the atomic mass unit, k the Boltzmann constant and S_{n+1} is the proton separation energy [12]. An analogy occurs for the isotopic chains in the neutron capture reactions of the r process.

Another way to describe the importance of the binding energy is found in the reaction rate

$$N_A \langle \sigma \upsilon \rangle = 1.540 \times 10^{11} (\mu T_9)^{-3/2} \times \sum_j \omega\gamma_j exp\left(\frac{-E_j}{kT}\right) \mathrm{cm^3 s^{-1} mole^{-1}}. \quad (2.2)$$

T_9 is the temperature in GK and μ is the reduced mass of the entrance channel in atomic mass units. $\omega\gamma_j$ is the resonance strength in MeV and E_j is the resonance energy in the center of mass system. [12] The resonance strength for proton capture is

$$\omega\gamma_j = \frac{2J_j + 1}{2(2J_\mathrm{T} + 1)} \frac{\Gamma_{\mathrm{p}j}\Gamma_{\gamma j}}{\Gamma_{\mathrm{total}j}}, \quad (2.3)$$

where J_T is the target spin, and $J_j, \Gamma_{\mathrm{p}j}, \Gamma_{\gamma j}$ and $\Gamma_{\mathrm{total}j}$ are the spin, proton-decay width, γ-decay width and total width of the compound nucleus state j. Eq. (2.2) is often the only way to determine reaction rates near the proton drip line because of low level densities limiting the use of statistical model calculations. Also, direct reaction rate measurements are still difficult, because they involve the use of radioactive isotopes.

Notably in Eq. (2.1) is that the proton separation energy is inside the exponent thus giving considerable weight to it and further to the mass difference between the parent and daughter nucleus. In Eq. (2.2) the atomic masses are also found inside the exponent in the form of the resonance energy. These exponential proportionalities lead to stringent requirements for the accuracy that the atomic masses should be known. The ground state masses and proton binding energies should preferably be known with an accuracy better than 10 keV.

The atomic masses are not the only significant paratemer that has to be known. For example, the half lives and the spins are essential. The nuclear spins play a role in defining the probability of nuclear processes whereas the half lives are important for creating seeds for capture reactions or so-called waiting points. If the half life is short it is possible to circumvent unbound nuclides and continue capture reactions via a new chain. Long half lives can create waiting points where the capture reactions can halt completely unless existing conditions make it possible to overcome the situation. An example of a waiting point in the rp process is ^{68}Se. The β-decay half life of this isotope is 35 s and ^{69}Br, the proton-capture daughter, is proton unbound. For the rp process to proceed in a time frame of an X-ray burst a two-proton capture is needed [13].

It has to be noted that the isotopes taking part in the stellar nuclear processes are not necessarily in their atomic ground states. Instead they can be in a higher charge state or in some cases even fully stripped. Also, the nuclides can be in excited states. This sets specific

requirements for the use of nuclear as well as atomic spectroscopy data in true astrophysical scenarios.

2.4 How to obtain the masses

2.4.1 Theoretical approaches

The nucleus of an atom can be described in two extremes. Either the nucleus is seen as whole, being a small charged liquid, solid or gaseous sphere that has strict boundaries, the macroscopic approach. Microscopic approaches start from the interactions between nucleons and builds the nuclide from the bottom up. Evidence for an atom to have a charged nucleus was shown by Ernest Rutherford in the early 20th century with the famous backscattering experiment on gold foils.

During the first half of the 20th century the nucleus was found to consist of two different types of particles: protons and neutrons. It was also found that the mass of an atom is not purely the sum of its building blocks, the nucleons and electrons. Instead a mass defect was observed, which was then interpreted as the binding energy of the nucleus. Thus the binding energy of an atom with Z protons and N neutrons can be written

$$B(Z,N) = (Z \cdot m_p + N \cdot m_n + Z \cdot m_e - M(Z,N))c^2. \tag{2.4}$$

Here m_p, m_n and m_e are the masses for the proton, neutron and electron, respectively, and $M(Z,N)$ is the total mass of an atom while c is the speed of light.

With systematic measurements throughout the nuclide chart the nuclei were found to be most bound in the region of iron. The nuclides above have a gradually decreasing behavior of the binding energy and the nuclides below noticeably faster. This gives the possibility of releasing energy by fusing two light nuclides or breaking a heavy one. To understand the behaviour of the binding energy of the nuclide it can be estimated to behave linearly as a function of the number of nucleons. Because of the linear dependence (instead of quadratic) and because the nuclear density has been found to be roughly constant, the nucleons must be attracting only the closest neighbour it has and each nucleon affects the same amount to the binding energy.

The nucleons on the surface of the nuclide do not have as many neighbours as those inside the volume. Therefore a correction has to be made. A further correction arises from the Coulomb repulsion of the protons. These two corrections with the linear estimation above give the liquid drop interpretation for a spherical nuclide.

Still these effects are not enough to explain the behaviour of the binding energy. The nuclides seem to consist of somewhat equal number of protons and neutrons. Also, it seems that similar nucleons like to couple in pairs. Adding these corrections to the liquid-drop

interpretion give the so-called liquid-drop model. The model is semiempirical in nature because each term has a parameter that is found by fitting to experimental values.

If the liquid-drop approach for modelling nuclei is macroscopic then a completely microscopic approach is to have suitable interactions between each nucleon. Trying to solve the equations quickly backfire in the form of many-body problems in nuclides larger than two nucleons, which are real pain to solve.

Great success of the shell model in atomic theory has emboldened nuclear theorists to apply similar approaches for nuclear structure. Here nuclear shells are filled with single particles in a way which satisfies the Pauli exclusion principle. This is another form of a microscopic model. Evidence for a shell-like structure of the nuclides are multifold. For example, two-proton and two-neutron separation energies have atomic shell like behaviours having a gradual increase in the energy as a function of nucleon number and a sudden drop when a "magic number" is crossed. By modifying the interaction between nucleons, different shell structures are attained. The excited state of a nuclide can be calculated by moving a nucleon to a different shell.

For the moment the best results for atomic masses are reproduced by models that combine both macroscopic and microscopic approaches. One of these hybrids is the finite-range droplet model (FRDM) [14]. The macroscopic part of the model has been modified from the liquid drop model so that it takes into account volume, surface and Coulomb effects of the nuclide. The number of correction terms in the FRDM is higher than in the classical liquid-drop model. Additional terms consist of, for example, curvature energy and a Wigner energy. The "finite range" in the name of the model indicates the restricted range of the nuclear forces. The microscopic part includes the Strutinsky shell correction and a pairing correction using the Lipkin-Nogami approximation. The finite-range droplet model has become a standard mass model that is used as a reference both for other models as well as for experiments. A concise description of the model can be found in the review article of Lunney *et al.* [15].

At present, the modelling and mass extrapolations do not give accurate enough results for the needs of stellar nucleosynthesis calculations. Therefore, direct experimental values are hungered for.

2.4.2 Experimental approaches

Conventionally the mass measurement techniques of radioactive isotopes are divided into two categories; indirect and direct methods. The indirect methods are mainly comprised of reaction and decay energy measurements. The reaction measurements can provide very precise results but the techniques involved are limited by the knowledge of incoming and outgoing particles along with the target mass. Measuring decay Q values can give precise mass differences but the results have to be linked to a known mass if a mass value is required.

This might result in accumulated errors, especially if the link is far away. Also, incomplete spectroscopic information can lead to incorrect Q-value determination.

The most precise direct methods of measuring the ion masses are governed by time-of-flight or frequency measurements. The simplest method of obtaining the time-of-flight is just to pass ions through an isochronous path. This method is in principle only limited by the length of the flight time and flight distance. Building a high precision, single pass apparatus is however not practical. By combining the time-of-flight measurement with a magnetic rigidity measurement, for example presented in Ref. [16], higher precision can be achieved. At best, the method is capable of producing a precision of around 100 keV as illustrated by SPEG in GANIL [17]. A clear benefit of the method is that it is applicable for isotopes with very short half-lives restricted by the survival of the isotopes across the flight path.

In connection with the time-of-flight method for mass determination, some other means than just a straight flight channel can be used to increase the effective path length. For example, the GANIL CSS2 cyclotron has been used to determine masses around $Z = N = 40$ [18]. The uncertainty of the results is around 100 keV. Another way to increase the effective flight path is to reflect the ions between two points several times as is done in multi-pass time-of-flight spectrometers (MTOF). Such a device is being developed to be used either for mass measurements of radioactive ions or only to be used as a mass separator [19–21].

Multiple passes of ions through a detector and thus an accumulating number of detections can be achieved by curving the flight path into a circle. An example of this is the ESR (Experimental Storage Ring) which can reach relative uncertainties of $\delta m/m \sim 10^{-7}$ [22]. This uncertainty corresponds at mass $A = 100$ to an energy of roughly 100 keV. This is not quite precise enough for the nucleosynthesis modelling but the technique has a clear advantage in that large mass regions can be measured in a short time. The downside is that the technique involves a complicated analysis process and a set of well-known reference masses with similar magnetic rigidities.

Instead of a direct time-of-flight measurement, the relation for the angular cyclotron frequency, $\omega_c = qB/m$, is commonly used. The most precise method today exploiting the cyclotron frequency technique is to use a Penning trap. The Penning trap combines static quadrupole electric fields to store the ions within a homogenous, several tesla magnetic field. Two ways to determine the frequency are used: Time-of-flight and Fourier-transform ion-cyclotron-resonance (FT-ICR) technique. With the time-of-flight technique the ions are excited within the trap and extracted. Depending on the excitation and ion mass the flight time differs. The FT-ICR technique relies on detecting the ions inside the trap via the electric signal they induce on detectors placed at a fixed position when the ions pass close to them. Another way is to first excite the ions with a RF electric field and let the ions directly hit a detector. The FT-ICR technique is mostly used for the mass measurement of stable elements but also in chemistry for molecular studies. The mass measurement of radioactive isotopes is primarily performed with the time-of-flight method.

With Penning traps relative uncertainties of $\delta m/m \sim 10^{-8}$ are achieved routinely for radioactive isotopes. For stable elements two orders of magnitude better than this has been reached. Examples of this are the facilities SMILETRAP [23] and Florida trap [24]. To achieve these uncertainties the measurement apparatus has to be known very well. For identifying possible systematic effects of the Penning trap spectrometer a carbon-cluster ion source can be used, as has been previously demonstrated in Refs. [25] and [26].

3 Experimental method

3.1 Production of neutron-deficient isotopes at IGISOL

To produce neutron-deficient isotopes, those on the left side of stability of the Segré chart, one has to produce a sufficiently high energy compound nucleus that breaks up into suitable fragments. At IGISOL this is done via light-ion or heavy-ion fusion-evaporation reactions. The light ion can be anything from a proton to an α-particle and, in principle, the heavy ion is only restricted by the capabilities of the primary beam production. The restrictions for the target material arise from those elements that can be made into a thin foil either self-supporting, within a compound or as a sufficiently thick layer on top of a backing foil.

A schematic layout of the full IGISOL and JYFLTRAP setup is shown in Fig. 3.1. The primary beam from the K-130 cyclotron hits the thin target in the IGISOL chamber. Reaction products are stopped in helium gas of the order of 200 mbar pressure and the (mainly) $q = 1+$ ions are extracted through an exit hole with a diameter of about 1 mm.

In this work both the light-ion and the heavy-ion ion guides were used. In the light-ion ion guide shown in Fig. 3.2 the target is directly connected to the ion guide. Before impinging on the target, the primary beam enters the ion guide through a beam window, usually made of Havar. The stopping gas volume of the guide is a few cm^3. The ion guide can have two different targets installed simultaneously and they can be exchanged by rotating the chamber through 180°. The primary beam passes through the whole ion guide and is stopped in a beam dump downstream.

In the heavy-ion ion guide setup shown in Fig. 3.3 the primary beam first hits a rotating target. Due to the kinematics, the reaction products fly from the target in a cone through a beam window (again usually Havar or in some cases nickel) of about 5 cm diameter and are stopped in a helium gas chamber that has a volume of a few 100 cm^3. In the heavy-ion ion guide the primary beam is stopped before the gas chamber in a graphite cylinder ($\oslash$7 mm) to prevent ionization of the buffer gas.

Following extraction from the gas cell the ions are guided through a sextupole ion beam guide (SPIG) [27] to a 30 kV extraction electrode and a 55° dipole magnet that has a mass resolving power of R$\leq$500. This resolving power is sufficient to separate ions with different mass over charge (m/q) from each other. After mass separation the ions enter the high-voltage platform of the JYFLTRAP setup.

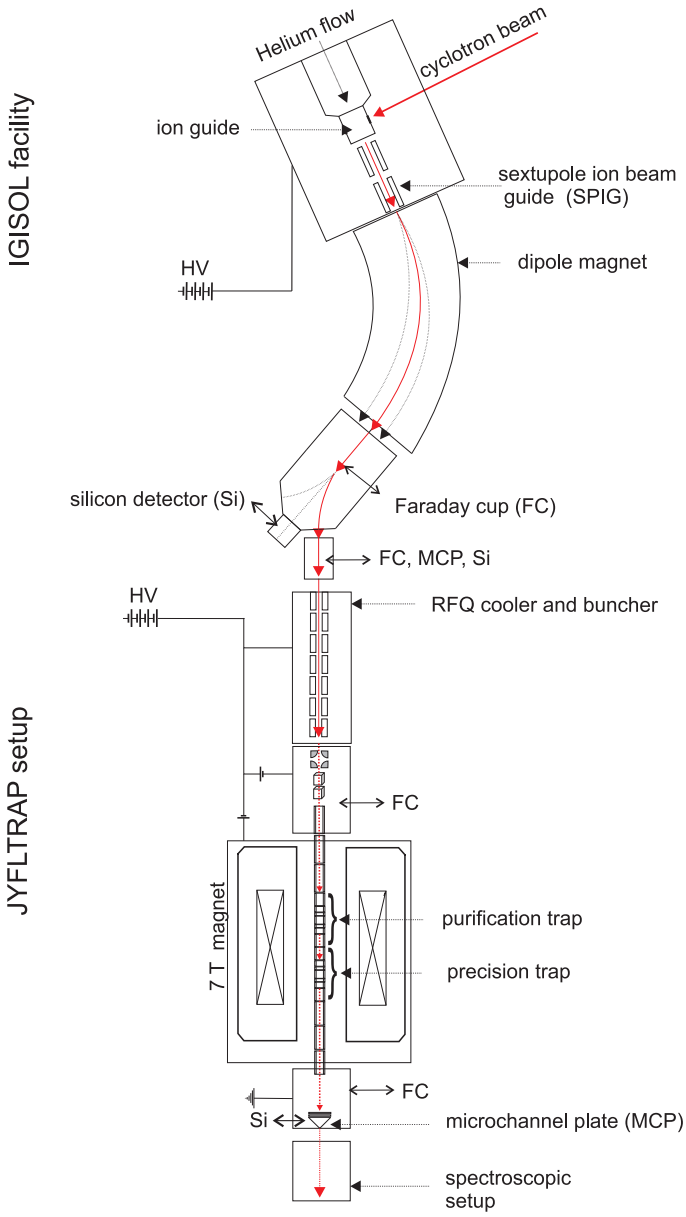

Fig. 3.1: A schematic layout of the IGISOL setup.

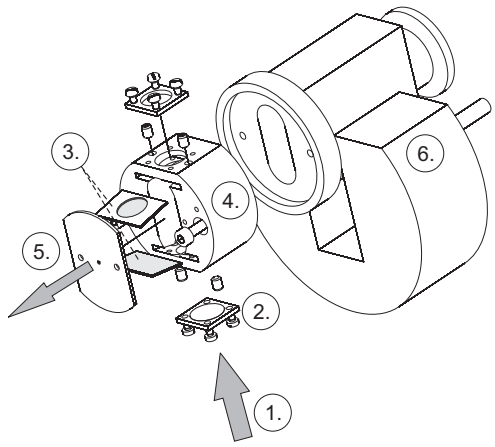

Fig. 3.2: A detailed view of the light-ion ion guide. (1) Primary beam from the K130 cyclotron, (2) thin beam window, (3) targets, (4) gas chamber, (5) reaction products extracted through a small (order of 1 mm) exit nozzle, (6) cooling element.

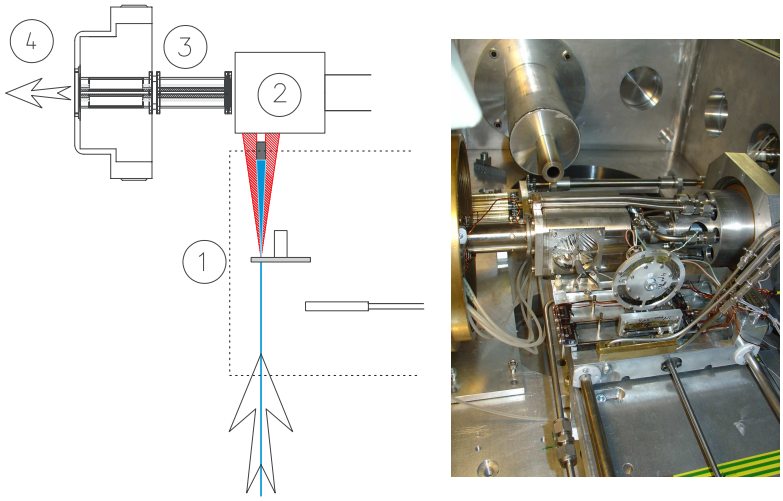

Fig. 3.3: A schematic view of the heavy-ion ion guide and a photograph. The primary beam hits a rotating target (1) and a cone of reaction products enter the gas cell (2) through a thin window. The primary beam is stopped to a graphite beam dump. The reaction products are extracted with the gas flow through the sextupole ion-guide SPIG (3) to mass separation and experiments (4).

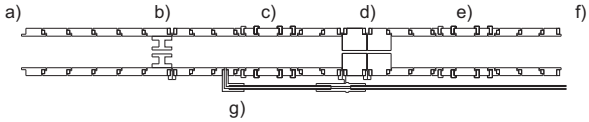

Fig. 3.4: A technical drawing of the Penning trap electrode structure. a) Injection to the trap; b) 4 mm diaphragm; c) the purification trap; d) 5 cm long, 2 mm diaphragm; e) the precision trap 20 cm separate from the purification trap; f) extraction to measurement setup; g) buffer gas inlet.

3.2 JYFLTRAP and the principle of the Penning trap technique

3.2.1 The JYFLTRAP setup in short

The JYFLTRAP setup consists of a radio-frequency cooler and buncher (RFQ) [28] and a double Penning trap situated in the warm bore of a 7 T magnet. First the ions are injected into the RFQ, a helium-gas filled Paul trap, where the ions are cooled in the buffer gas and are extracted to the Penning trap setup in the order of 15 μs bunches. The buffer-gas filled first trap is used for isobaric purification with the side-band cooling technique [29] and the second trap, having ultra-high vacuum, for precision mass measurements using the time-of-flight ion-cyclotron resonance technique (TOF-ICR) [30]. A technical drawing of the electrode structure of the Penning traps is illustrated in Fig. 3.4.

3.2.2 Ion motion in a Penning trap

A Penning trap consists of a homogenous magnetic field and a static quadrupole electric field. The magnetic field defines the z-axis of the trap and it confines the ions in x- and y-directions. The electric fields are used to confine the ions in the z-direction.

In a magnetic field $\vec{B}$ ions with charge q and velocity $\vec{v}$ feel a force

$$\vec{F} = q\vec{v} \times \vec{B}. \tag{3.1}$$

In the magnetic field of strength B, the ions with mass m will move in a circular motion around the magnetic field lines with angular frequency (or angular velocity)

$$\omega_{\mathrm{c}} = \frac{qB}{m} = 2\pi\nu_{\mathrm{c}}. \tag{3.2}$$

Here ν_{c} is the cyclotron frequency.

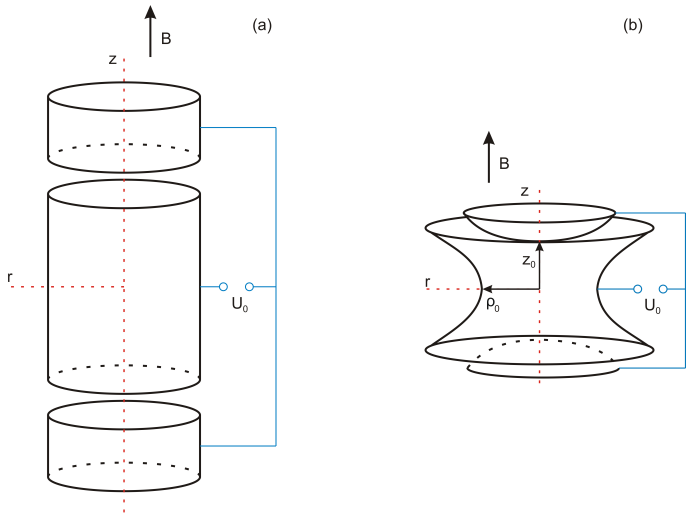

Fig. 3.5: Different electrode structures, cylindrical (a) and hyperbolic (b). The ring electrode is in the middle and end caps above and below it.

The shape of a quadrupole electric field in cylindrical coordinates is

$$U(z,\rho) = \frac{U_0}{d^2}\left(z^2 - \frac{\rho^2}{2}\right), \tag{3.3}$$

where

$$d = \sqrt{\frac{z_0^2 + \rho_0^2/2}{2}} \tag{3.4}$$

is the characteristic trap dimension. U_0 is the potential difference between the ring electrodes and the end caps, ρ_0 and z_0 are the orthogonal distances from the middle of the ring electrode to the inner surface of the ring electrode and the end caps, respectively.

Two types of electrode structures are used to create the required quadrupolar field, see Fig. 3.5. They are hyperbolic or cylindrically symmetric electrodes consisting of a ring electrode and end caps. With the hyperbolic electrodes the quadrupole field geometry can be defined more accurately. The advantage of the cylindrical electrodes is that their construction and use are simpler, in particular for the injection and extraction of ions. The quadrupole field is refined with correction electrodes. Hyperbolic electrodes are used for example at ISOLTRAP [31] and SMILETRAP [32] whereas the cylindrical type has been the choice for JYFLTRAP.

Equation 3.3 consists of electric field components

$$E_z = -\frac{U_0}{d^2} z \tag{3.5}$$

and

$$\vec{E_\rho} = -\frac{U_0}{2d^2} \vec{\rho}. \tag{3.6}$$

By having the magnetic field in the z-direction

$$\vec{B} = B\hat{e}_z, \tag{3.7}$$

the equations of motion for an ion with mass m and charge q are

$$\ddot{z} = \frac{q}{m} E_z \tag{3.8}$$

and

$$\ddot{\vec{\rho}} = \frac{q}{m}(\vec{E_\rho} + \dot{\vec{\rho}} \times \vec{B}). \tag{3.9}$$

The first of these describes the harmonic oscillation in the direction of the magnetic field with angular frequency

$$\omega_z = \sqrt{\frac{qU_0}{md^2}} \tag{3.10}$$

and the second in the radial plane with angular frequencies

$$\omega_\pm = \frac{\omega_c}{2} \pm \sqrt{\frac{\omega_c^2}{4} - \frac{\omega_z^2}{2}}, \tag{3.11}$$

where ω_c is again the angular cyclotron frequency as in Eq. (3.2). The three eigenmotions are presented in Fig. 3.6.

Between the angular cyclotron frequency, ω_c, magnetron frequency, ω_-, reduced cyclotron frequency, ω_+, and axial frequency, ω_z, the following relations are valid

$$\omega_c^2 = \omega_+^2 + \omega_-^2 + \omega_z^2 \tag{3.12}$$

$$\omega_c = \omega_+ + \omega_- \tag{3.13}$$

$$\omega_z^2 = 2\omega_+\omega_- \tag{3.14}$$

$$\omega_c > \omega_+ > \omega_z > \omega_-. \tag{3.15}$$

The first of these relations is the so-called invariance theorem [33] which holds even if there is a misalignment between the magnetic and electric field axis or a higher-order distortion in the electric quadrupole field [34]. The second equation – Eq. (3.13) – is a sideband frequency of the invariance theorem and is exactly valid only in an ideal Penning trap. In practice it is often enough to use Eq. (3.13) for cyclotron frequency determination. The reason for this arises from the invariance theorem because systematic shifts turn out to be small compared to the precision needed. See for an explanation and justification in Ref. [34] or for a slightly more detailed explanation in Ref. [35].

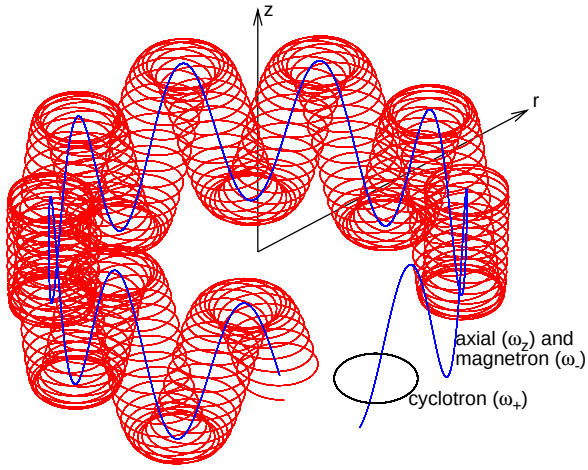

Fig. 3.6: Ion motion in the Penning trap.

3.2.3 Capturing ions

Capturing of the ions into the Penning trap is done by lowering the potential wall on the injection side of the trap to a level below the ion kinetic energy. After a short time, depending on the mass of the ions, the injection wall is closed. The release of the ions is performed by lowering the extraction side wall. A graphical explanation is shown in Fig. 3.7. The potential depths of the JYFLTRAP setup are 100 V in the purification trap and 10 V in the precision trap.

The time needed to have the wall open depends on the mass of interest. The heavier the mass the longer the time-of-flight and thus a longer open time is needed. The time-of-flight of the ions from the RFQ to the first Penning trap varies between 50–150 μs while the time-of-flight between the two Penning traps is between 25–100 μs. After the ions are inside the trap the wall has to be closed within about 2 μs so that the ions won't have time to be reflected backwards out of the trap.

3.2.4 Dipole excitation

By dividing the ring electrode into quadrants, see Fig. 3.8, it is possible to create an oscillating dipole or quadrupole field in the middle of the trap. With a magnetron radio frequency the amplitude of the magnetron motion for all the ions in the trap can be linearly increased. The optimal magnetron frequency for an ideal trap can be calculated from equations 3.10,

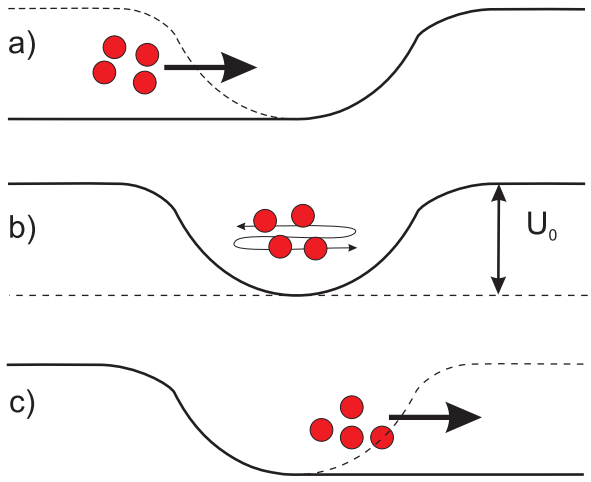

Fig. 3.7: Injection (a), capture (b) and release (c) of ions in the Penning trap by lowering and raising of the potential walls. U_0 is the trapping potential.

3.11 and 3.2. In the case of JYFLTRAP, the optimal magnetron frequency for the purification trap is roughly 1700 Hz and for the precision trap about 180 Hz.

Because the magnetron frequency is small compared to the cyclotron frequency the electric field part ($q\vec{E}$) of the Lorentz force

$$\vec{F_L} = q(\vec{E} + \vec{v} \times \vec{B}) \tag{3.16}$$

dominates for the magnetron motion while for cyclotron motion the magnetic field part dominates. The result is that the effect of magnetron excitation is almost mass independent, whereas excitation with reduced cyclotron frequency is mass selective. Thus, such excitations can be used accordingly.

3.2.5 Quadrupole excitation

The magnetron and reduced cyclotron motions can be coupled with quadrupole radiofrequency excitation. In excitation with a frequency corresponding to the cyclotron frequency of a certain mass, the energy of magnetron motion can be transferred to reduced cyclotron motion. In this exchange the radius of reduced cyclotron motion is increased while the magnetron radius decreases. By extending the time of excitation the conversion can be interchanged. By tuning the excitation amplitude corresponding to excitation time it is possible to make only one full conversion from magnetron motion to reduced cyclotron motion. The

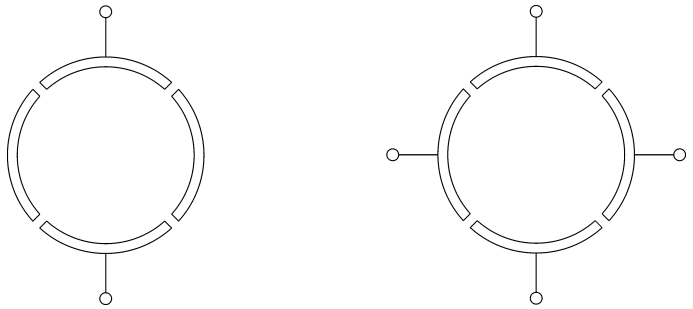

Fig. 3.8: The ring electrode structure of a Penning trap. At left is the dipole and at right the quadrupole configuration.

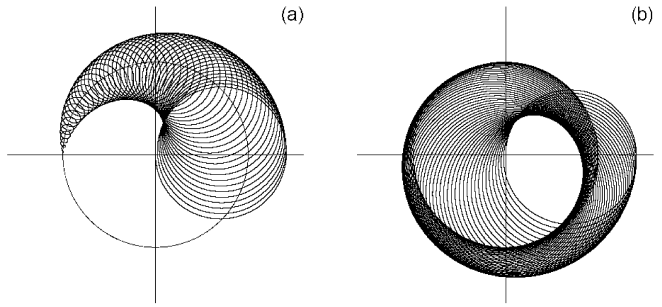

Fig. 3.9: The conversion of magnetron motion into reduced cyclotron motion in quadrupole excitation; a) first half, b) second half.

conversion of the ion motion made in high vacuum is illustrated in Fig. 3.9. For a singly-charged ion of mass $A = 100$ in a 7 T magnetic field the cyclotron resonance frequency is of the order of 1 MHz.

In practice two different excitation schemes can be used in Penning trap mass spectrometry. In a conventional scheme the quadrupole excitation is applied with constant amplitude before extracting the ions from the trap. Another method is to use so-called time-separated oscillatory fields, called Ramsey excitation. Here the quadrupole excitation is divided into two (or more) periods, fringes, having a time between them when no excitation is applied. Fig. 3.10 displays the difference of radial motion conversion between the conventional excitation scheme and a two-fringe excitation. In the figure the ions have only magnetron motion in the beginning of the excitation and the ions are in high vacuum, thus not experiencing any

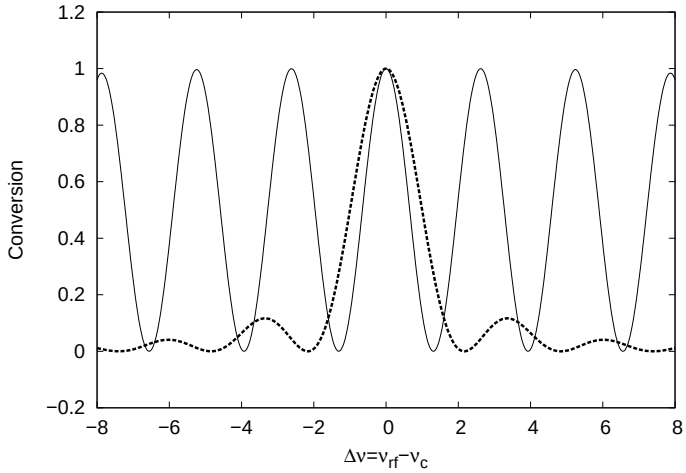

Fig. 3.10: Conversion between the two radial eigenmotions in an ideal trap as a function of detuned frequency. For the conventional method (dashed line) a 400 ms excitation pattern was used and for Ramsey excitation (solid line) two 25 ms excitation fringes were applied having a 350 ms waiting time between.

damping of motions. In the conventional scheme the quadrupole excitation time is 400 ms and in the Ramsey scheme the fringes are 25 ms long having a 350 ms waiting time between them. For one full conversion at the resonance frequency the excitation amplitude is scaled with a factor

$$(T_{RF} + T_{wait})/T_{RF}. \tag{3.17}$$

Here T_{RF} is the excitation time and T_{wait} the waiting time. With the Ramsey method the resonance width can be reduced by up to 40 %.

3.2.6 Buffer gas cooling and principle of purification trap

Before the dipole or quadrupole excitation is effective the ion bunch has to have minimum excess energy. A powerful way to damp the axial motion is buffer gas cooling. For this, helium is usually used as the gas because of its light mass and high ionization potential. In the buffer gas the radius of the reduced cyclotron motion gets smaller while the magnetron radius is increased. The effect on the magnetron motion is slower than the effect on the reduced cyclotron motion (Fig. 3.11a)). At JYFLTRAP, depending on the half-life of the ion of interest and mass, this so-called axial cooling is done for 50 to 200 ms. Of course, by changing the helium pressure the effectiveness changes. A typical pressure in the

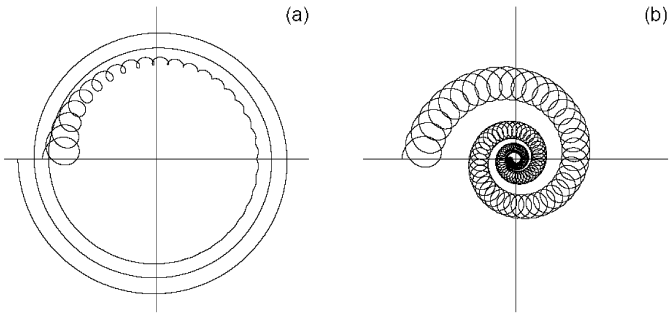

Fig. 3.11: Ion motion in buffer gas a) without quadrupole excitation and b) with excitation on the resonance frequency.

purification trap is of the order of 10^{-4} mbar.

To start a mass-dependent radial motion conversion, big enough magnetron radius just before the conversion is needed. In order to move the ions to such radius, a short magnetron (dipole) excitation must be applied. At JYFLTRAP, the duration of the magnetron excitation is of the order of 10 ms with an amplitude ranging from 200 mV to 800 mV.

In high vacuum, the quadrupole excitation at the correct frequency converts radial motions of a certain mass from one to another. This is still true if there is buffer gas present, but the constant cooling effect changes the ion motion, which results in re-centering the ions of a given mass. The ion motion in buffer gas with a quadrupole excitation is illustrated in Fig. 3.11b). The amplitude for the cyclotron excitation at JYFLTRAP ranges from 100 mV to 500 mV having an excitation time of 50 to 300 ms.

Before the ions are finally released to the precision trap approximately 10 to 50 ms radial cooling time is needed after the excitations. If the purification trap is used for mass selective ion counting purposes the extra radial cooling is not always used. Also, in that case the ions are not trapped in the precision trap but only transferred through for detection with micro-channel plates (MCP).

Different resolving powers can be achieved by using different amplitudes, excitation times and buffer gas pressure. For high mass resolution usually a lower gas pressure coupled with longer excitation times and smaller initial bunch size are needed. To maximise transmission the resolution has to be compromised. Then higher buffer gas pressure and bigger bunch sizes are used. The highest resolution ($\Delta\nu_{FWHM}$) achieved with the purification trap of the JYFLTRAP setup has been slightly better than 10 Hz. For singly charged ions of mass 100 this corresponds to a mass resolving power of the order of $R \sim 10^5$. Normally the resolution

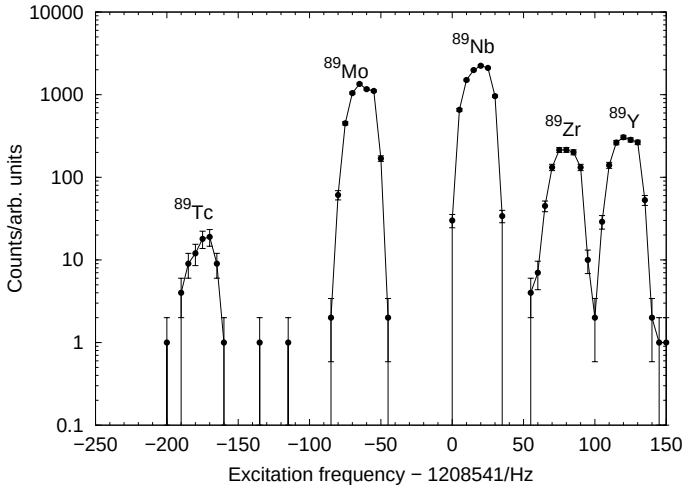

Fig. 3.12: Frequency scan performed in purification trap for mass $A = 89$. The isobars were produced in proton-induced reactions at a beam energy of 62 MeV on a molybdenum target.

during a mass measurement is between 20–30 Hz. An example of a typical purification scan is shown in Fig. 3.12. A schematic example of a purification pattern, part of a full mass measurement scheme, is seen in Fig. 3.13.

3.2.7 Precision trap, from time-of-flight to mass

In an ideal situation the ions are trapped in the precision trap with a minimal excess of radial and axial energy. In a precision mass measurement at JYFLTRAP the well-centered ions are again first excited with a dipole excitation to a larger magnetron radius. The ions are then excited with a quadrupole excitation to convert the magnetron motion to reduced cyclotron motion either with a conventional or Ramsey excitation scheme before extracting the ions to the MCP detector for TOF-ICR (time-of-flight ion-cyclotron resonance) measurement [30].

Another use for the precision trap, adopted at JYFLTRAP, is the so-called Ramsey purification where the purification power of the JYFLTRAP system can be increased by a factor of about ten [36, 37]. Fig. 3.13 shows an example of a typical timing pattern used in a mass measurement. The figure is slightly simplified because in the real situation the purification and precision trap can be operated simultaneously or in some cases additional purification via the Ramsey cleaning method might be used (see references above).

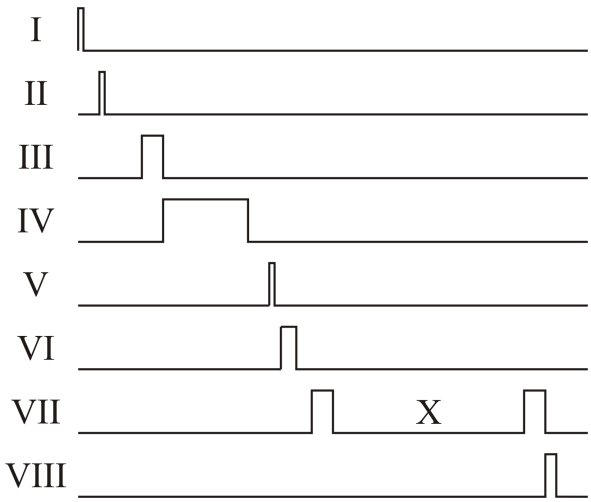

Fig. 3.13: An example of a typical timing pattern used during a mass measurement. Not in scale. I) Extraction from RFQ ($\sim 15\mu$s); II) Injection to purification trap after transfer; III) Magnetron excitation of the order of 10 ms after $50 - 200$ ms axial cooling; IV) Conversion to reduced cyclotron motion with quadrupole excitation of $50 - 300$ ms; V) Transfer from purification trap to precision trap (tens of μs); VI) Magnetron excitation of about 5.5 ms; VII) Quadrupole excitation for motion conversion with two-fringe Ramsey excitation pattern, conventional excitation without having the space X in between; VIII) Extraction to MCP.

After the quadrupole excitation the ions are extracted from the trap for time-of-flight detection. The ions with cyclotron motion have a radial kinetic energy of $E_\rho(\omega_{\rm rf})$. When these ions interact with a magnetic field of $\vec{B} = B\hat{e_z}$ their magnetic moment is

$$\vec{\mu} = \frac{E_\rho(\omega_{\rm rf})}{B}\hat{e_{\rm z}}. \tag{3.18}$$

When these ions drift out of the trapping region though the gradient of the magnetic field, they experience a longitudinal force

$$\vec{F}(\omega_{\rm rf}, z) = -\vec{\mu}(\omega_{\rm rf}) \cdot \left(\nabla \vec{B}(z)\right). \tag{3.19}$$

This force converts radial kinetic energy into axial kinetic energy. In the trap, the ions undergoing a pure reduced cyclotron motion have also maximal possible radial kinetic energy. Those ions having only magnetron motion have minimum radial energy. This is because the kinetic energy is proportional to ν^2 and the radial frequencies have the hierarchy of Eq. (3.15). Thus the ions who have experienced a full conversion of radial motion from magnetron to reduced cyclotron experience the gradient the strongest. This gives a maximum velocity and therefore minimum time-of-flight.

For the conventional excitation pattern Ref. [38] and for the Ramsey scheme Ref. [39, 40] the time-of-flight can be calculated with an integral

$$T(\omega_{\rm rf}) = \int_{z_0}^{z_1} \sqrt{\frac{m}{2[E_0 - qU(z) - \mu(\omega_{\rm rf})B(z)]}}dz. \tag{3.20}$$

Here E_0 is the initial, total kinetic energy of the ions and U(z) and B(z) the electric and magnetic fields along the path of the ions from the center of the trap (z_0) to the detector (z_1). For a more detailed description of the measurement and fitting procedure used at JYFLTRAP see Ref. [2]. In Fig. 3.14 examples of time-of-flight ion-cyclotron-resonance (TOF-ICR) scans done at the JYFLTRAP setup are shown.

The mass of the atom of interest, $m_{\rm meas}$, is

$$m_{\rm meas} = r \times (m_{\rm ref} - m_{\rm e}) + m_{\rm e}. \tag{3.21}$$

Here $m_{\rm ref}$ is the mass of the reference atom, $m_{\rm e}$ is the mass of an electron. The electron binding energy is neglected. The frequency ratio, r, between the ion of interest and the reference ion is

$$r = \frac{\nu_{\rm c,ref}}{\nu_{\rm c}}. \tag{3.22}$$

The frequency ratio is the primary experimental observable because it is independent on the pre-existing information on the reference mass.

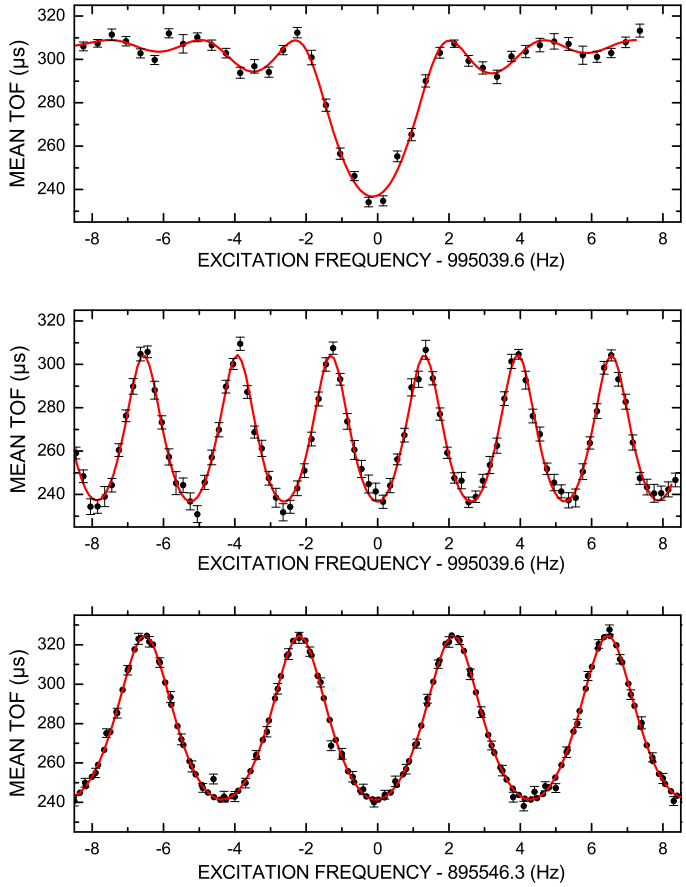

Fig. 3.14: Examples of TOF-ICR resonance scans done at JYFLTRAP with carbon clusters. The topmost panel is performed with a 400 ms conventional excitation pattern with $^{12}C_9^+$ ions, the middle with 25-350-25 ms two-fringe Ramsey pattern also with $^{12}C_9^+$ ions and the bottom with 25-200-25 ms two-fringe Ramsey pattern with $^{12}C_{10}^+$ ions.

3.3 Recipe for obtaining the uncertainties in the mass measurement

Determining the center frequency

The center frequency, ν_c, and the statistical uncertainty are obtained from a theoretical fit [38, 40, 41] to the experimental time-of-flight data. The center frequency may shift if the precision trap has contaminant ions present. This is typically corrected by doing a count-rate class analysis [25]. In the count-rate class analysis the data are divided into at least three classes with similar statistics. Their center frequencies are obtained in individual fits and the final result is extrapolated to a value corresponding to one ion stored in the trap. Another way is to restrict the count rate per bunch to a fixed low number.

Effect of magnetic field changes

Determination of the wanted frequency is done by doing a measurement with a reference ion before and after the ion of interest and interpolating their value to the time of the measurement. From the fitted center value the frequency ratio $r = \nu_{\mathrm{c,ref}}/\nu_{\mathrm{c}}$ is calculated. In addition to the linear drift of the magnetic field, random, time-dependent fluctuations of the B-field have to be taken into account. This is done by quadratically adding $\sigma_B(\nu_{\mathrm{c,ref}})/\nu_{\mathrm{c,ref}}$ to the uncertainty of each individual frequency ratio.

Birge ratio

For the final frequency ratio value a weighted average of each measurement set is calculated. The scatter of the data points compared to their individual uncertainties is studied by calculating the ratio of the inner and outer uncertainties (Birge ratio) [42]. This ratio should be close to one. To remain conservative, in this work the larger of the inner or outer value is taken as the final uncertainty.

Final uncertainty

To obtain the final uncertainty of the frequency ratio, two other uncertainties are quadratically added with the above value: the mass dependent effect, $\sigma_{\mathrm{m}}(r)/r$, and an unknown, residual effect, $\sigma_{\mathrm{res}}(r)/r$. The mass dependent effect arises from imperfections in the trapping fields [34, 43] whereas the reason for residual effect is unknown. Both of these effects at the JYFLTRAP setup have been investigated in this work with the help of a carbon-cluster ion source.

The effect of the reference mass uncertainty is taken into account only in the calculation of the mass of the atom of interest.

3.4 Carbon-cluster measurements

3.4.1 Motivation and theory

Carbon clusters are ideal for examining the systematic effects of Penning traps. First of all, they are available in equidistant steps over a broad mass range, in steps of 12 mass units, if the more abundant carbon isotope is used. Secondly, the mass of carbon clusters is almost purely the mass of multiple carbon atoms. A small correction comes from the molecular binding energies, but since they are only up to 7 eV per atom combined with the fact that there are no large, sudden jumps in the binding energy in clusters smaller than C_{60} [44], the correction is negligible in the accuracies of this work and can be discarded.

One of the systematic effects present in a Penning trap mass spectrometer depends on the measured mass – or, more precisely, the mass difference between the ion of interest and reference ion. This effect can arise due to imperfections of the electrostatic field of the Penning trap or misalignment between the magnetic and electric field axis [33, 34, 43]. To investigate the possible mass dependent effects of the JYFLTRAP system frequency ratios measured with carbon clusters can be compared to calculated ones. By assuming a constant frequency shift $\Delta\nu$ the measured frequency ratio can be written as

$$r = \frac{\nu_{\mathrm{c,ref}} + \Delta\nu}{\nu_{\mathrm{c}} + \Delta\nu}, \tag{3.23}$$

while the true calculated frequency ratio would be

$$r_{\mathrm{calc}} = \frac{\nu_{\mathrm{c,ref}}}{\nu_{\mathrm{c}}}. \tag{3.24}$$

From these equations a relation between the calculated and the measured frequency is

$$\frac{\epsilon(r)}{r} = \frac{r - r_{\mathrm{calc}}}{r} = \frac{\Delta\nu}{\nu_{\mathrm{c,ref}} + \Delta\nu}\left(\frac{m_{\mathrm{ref}} - m_{\mathrm{meas}}}{m_{\mathrm{ref}}}\right). \tag{3.25}$$

This is proportional to the mass difference of the reference atom and the atom of interest when taking note that $\Delta\nu$ is very small. With carbon clusters the performance of the Penning trap setup has been investigated at ISOLTRAP [25] and at SHIPTRAP [26]. To be able to compare to their work the proportionality is taken to be $m_{\mathrm{meas}} - m_{\mathrm{ref}}$.

If a mass-dependent effect is found, the data can be corrected with the obtained effect. After the correction the data can again be compared to the calculated frequency ratios with

$r_{\mathrm{corr}} - r_{\mathrm{calc}}$. If the reduced χ^2 for the obtained distribution for this is greater than one, either some of the uncertainties determined so far have been underestimated or there is still some residual uncertainty present.

3.4.2 The Carbon-cluster ion source and how it works

The carbon clusters are produced by ablating a Sigradur® carbon plate with a frequncy doubled 532 nm Brilliant, Q-switched, Nd:YAG laser. The laser operates with up to 10 Hz repetition rate. The 20×20×2 mm carbon plate is mounted on a rotating base to prevent the laser continuously firing at the same spot and thus burning a hole through the plate. The power of the laser is varied by changing the time between the firing of the flashlamp and opening of the Q-switch. Usually, after focusing the laser spot, an energy of a few mJ per pulse is needed to ablate enough cluster ions for the Penning trap measurement (the energy curve for the laser is in Fig. 3.15). The ionized clusters are extracted to the RFQ and the Penning traps with electric fields. See photographs in Fig. 3.17 of the setup and a Sigradur carbon plate after a two week test period. A detailed view of the carbon-cluster ion source is shown in Fig. 3.16.

As in all trap measurements the RFQ is first used to cool and bunch the ions before injecting them to the Penning trap system. Another advantage of injecting the carbon clusters into the RFQ is that it can, to some extent, be used for initial mass purification. The size of the carbon-cluster ions produced with laser ablation can not be controlled. Instead, the carbon cloud contains different species with quite a wide spectrum. In Fig. 3.18 the mass purifying properties of the RFQ are illustrated. The disadvantage of the location for the source is that a separate high-voltage platform had to be built. This creates a possibility for sparks if the electric insulations are not adequate, or at least the full high-voltage level of 30 kV can not be used.

In other Penning trap facilities where a carbon-cluster ion source has been used so far (ISOLTRAP, SHIPTRAP) the source is situated after the RFQ. At JYFLTRAP the carbon-cluster ion source was also tested in a similar place. The advantage was that no separate high voltage platform had to be built as it could be connected inside the same platform as the RFQ and trap to a quadrupole deflector. Also, instead of mechanical movement, only by building electric switches the beam from the ion-source and IGISOL could have been interchanged. Due to bad beam quality, however, the ion source was finally located in front of the RFQ. Moving the source all the way in to the IGISOL chamber was not feasible due to heavy usage of the IGISOL vacuum chamber for on- and off-line tests.

An extensive description of the carbon-cluster ion source and the development work done at JYFLTRAP can be found in references [45] and [46], both of which are added to the appendix of this thesis.

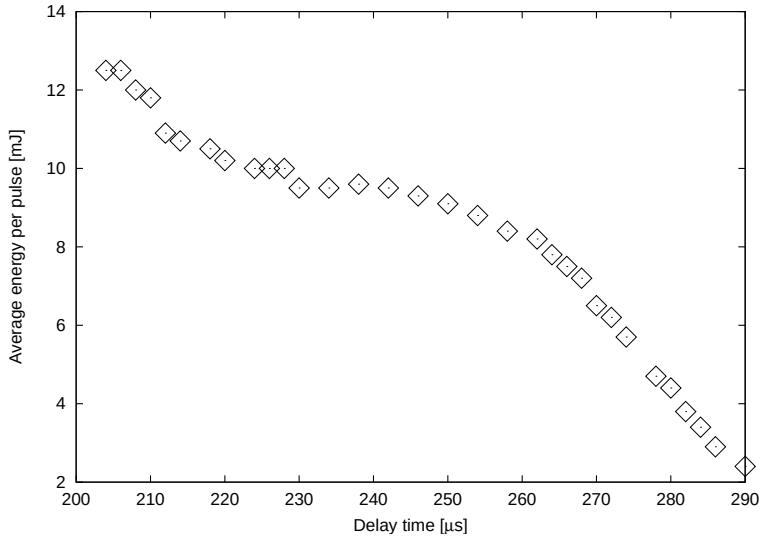

Fig. 3.15: Measured average energy per pulse of the Brilliant Ng:YAG laser with 10 Hz repetition rate. On the x-axis is the time between flashlamp and Q-switch. Diameter of the laser spot before focusing is roughly 5 mm.

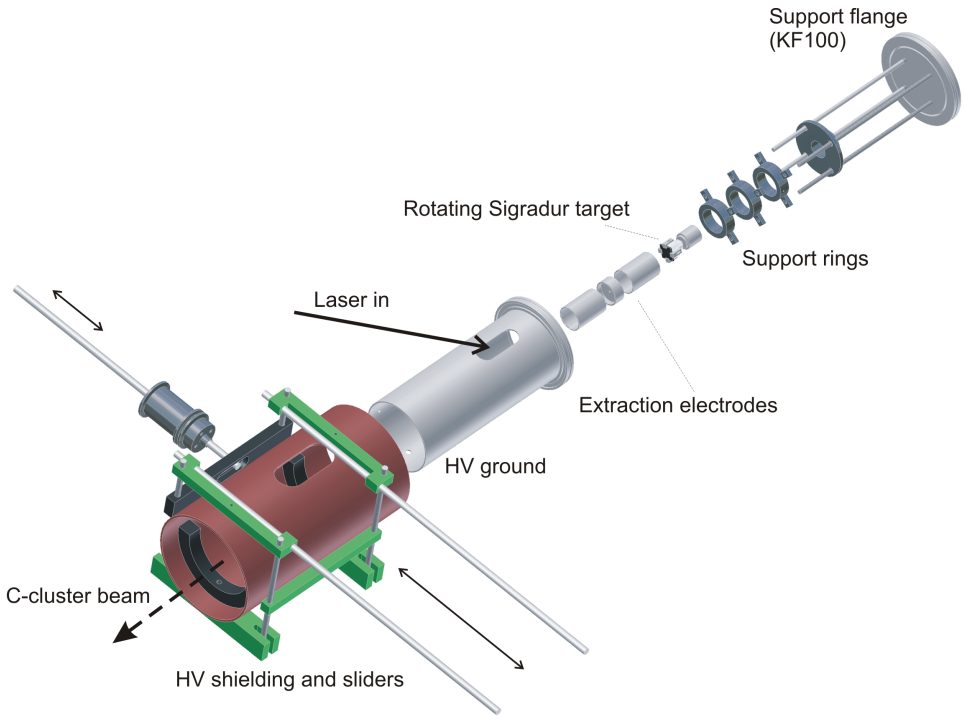

Fig. 3.16: Detailed view of the carbon-cluster ion source.

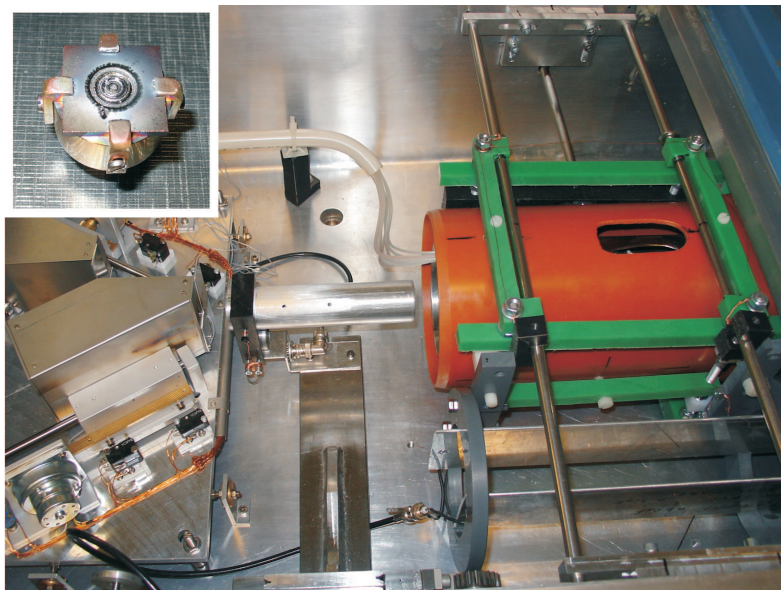

Fig. 3.17: Photo of the C-cluster source installed in the switchyard. In the upper corner the Sigradur® target after a two week run.

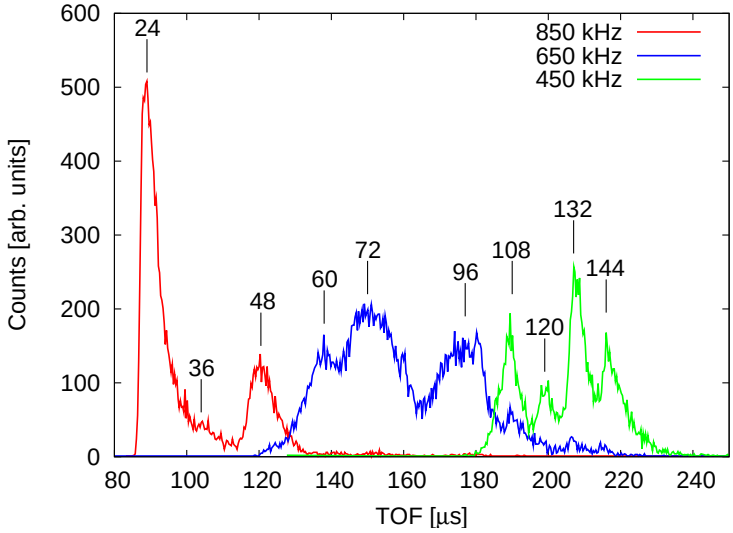

Fig. 3.18: Counts vs. time-of-flight for three different RFQ frequencies. For each TOF measurement about five carbon-cluster clouds were injected into the RFQ. After cooling, the cluster ions were released through the Penning traps to a MCP detector.

	$^{12}C_{meas}$	5	6	7	8	9	10	11	12	13	14	15	16	17
$^{12}C_{ref}$	A	60	72	84	96	108	120	132	144	156	168	180	192	204
7	84	16	10		9	13		10						
10	120		20	10	13	10		9	9	10	10			
13	156					10		10	10		20	20	10	10

Δm
-48
-36
-24
-12
12
24
36
48

Fig. 3.19: Overview on carbon-cluster cross-reference measurements done in this work.

3.4.3 C-cluster measurements and results

More than 200 cross-reference pairs divided into three reference clusters were measured. The measurements are summarised in Fig. 3.19. As reference masses cluster ions of $^{12}C_7^+$, $^{12}C_{10}^+$ and $^{12}C_{13}^+$ were chosen. Three of the measurement sets were performed two times, one having different purification trap settings ($^{12}C_6^+$ against $^{12}C_{10}^+$) and all on a different measurement day. Two different precision trap settings were used consisting of either 400 ms or 250 ms Ramsey excitation patterns having both 25 ms excitation fringes and a waiting time of 350 ms or 200 ms. The Ramsey excitation was preferred over conventional excitation because of the increased accuracy of the center frequency determination.

Theoretical fits [39] of the data were made, frequency ratios were calculated and the uncertainties were determined as explained in the publication [46]. With equation 3.25 the relative difference to the theoretical values were calculated. The obtained values can be illustrated in the form of ideograms [47] which are a sum of Gaussian functions having a center value calculated with Eq. (3.25) and a corresponding uncertainty as the width. The ideograms (Fig. 5 in publication [46]) themselves closely resemble a Gaussian distribution.

The relative differences to the theoretical values are plotted as a function of $m_{\mathrm{meas}} - m_{\mathrm{ref}}$ in Fig. 3.20. A mass-dependent effect of $\sigma_{\mathrm{m}}(r)/r = (7.8 \pm 0.3 \times 10^{-10}/u) \times \Delta m$ has been determined from a linear fit weighted with individual uncertainties. The measured frequency ratios can be corrected with this value and a possible residual effect can be investigated. Since the χ^2/N for the corrected values is found to be greater than one, the residual effect has to be taken into account. By quadratically adding a value of $\sigma_{\mathrm{res}}(r)/r = 1.2 \times 10^{-8}$ to the uncertainties of the final frequency ratios, the χ^2/N becomes one. The added residual uncertainty is illustrated in Fig. 3.21. The same data can be plotted as a function of the measured mass, instead of the mass difference. This is done in Fig. 3.22, where no more extra mass dependent effects can be seen.

The reference mass used at JYFLTRAP has never been further than about 20 mass units from the ion of interest. This justifies restricting the investigation into the mass difference range of ± 24. In this range the mass dependent effect is found to be $\sigma_{\mathrm{m,lim}}(r)/r = (7.5 \pm 0.4 \times 10^{-10}/u) \times \Delta m$ and the corresponding residual uncertainty is $\sigma_{\mathrm{res,lim}}(r)/r = 7.9 \times 10^{-9}$.

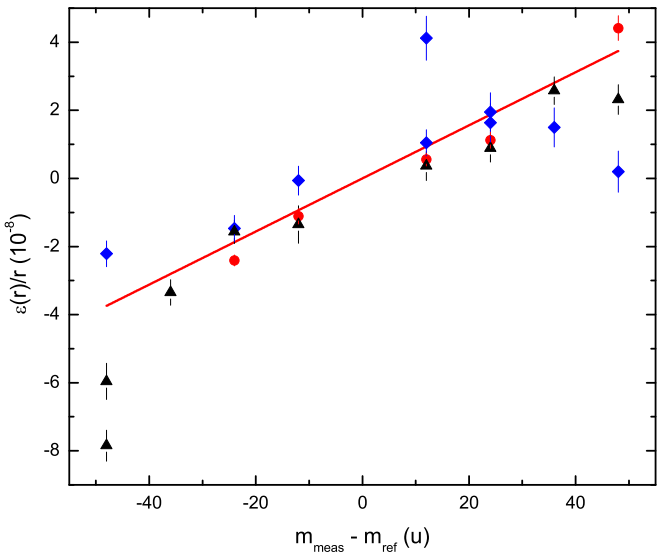

Fig. 3.20: Relative difference between the measured frequency ratio to the calculated one – Eq. (3.25) – as a function of $/Deltam = m_{\mathrm{meas}} - m_{\mathrm{ref}}$. The fitted mass dependent effect is $\sigma_m(r)/r = (7.8 \pm 0.3 \times 10^{-10}/u) \times \Delta m$. The red circles indicate the measurements performed with $^{12}C_7^+$, black triangles $^{12}C_{10}^+$ and blue diamonds $^{12}C_{13}^+$ as the reference ion.

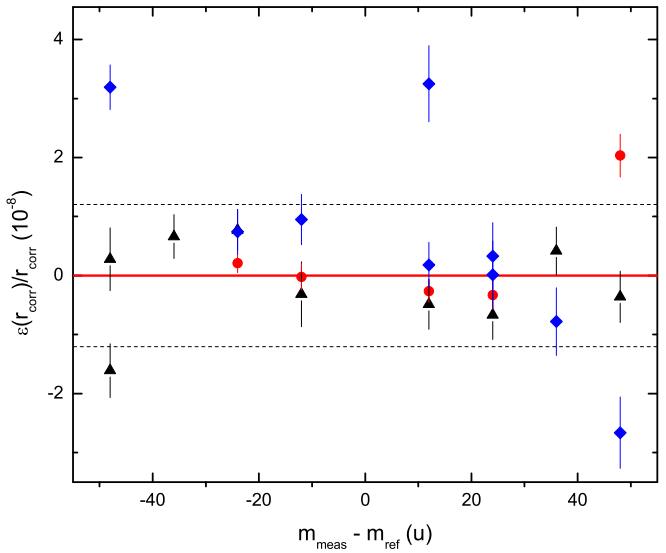

Fig. 3.21: Same data as in Fig. 3.20 after correcting for the mass dependent effect. The dashed lines indicate the residual error that has to be added to the uncertainties of the frequency ratios, $\sigma_{\mathrm{res}}(r)/r = 1.2 \times 10^{-8}$, to make $\chi^2/\mathrm{N} = 1$. The red circles indicate the measurements performed with $^{12}\mathrm{C}_7^+$, black triangles $^{12}\mathrm{C}_{10}^+$ and blue diamonds $^{12}\mathrm{C}_{13}^+$ as the reference ion.

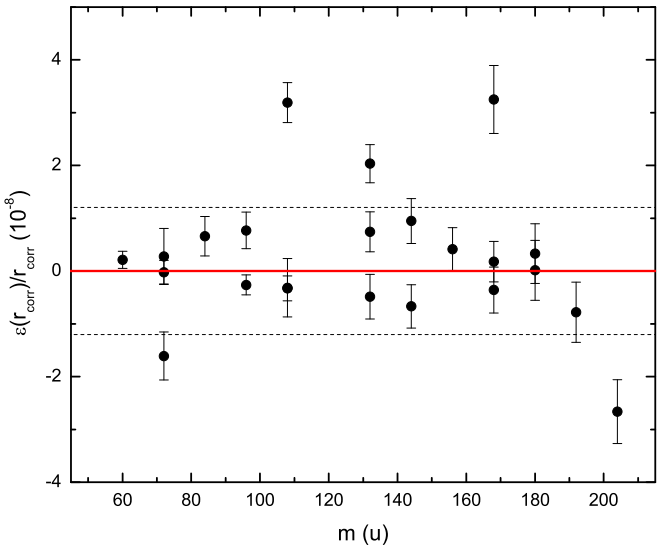

Fig. 3.22: Same data as in Fig. 3.21, however plotted against the measured mass.

3.4.4 Summary of C-cluster measurements

The carbon-cluster ion source was built, tested and used for quantifying the mass dependent effect and residual uncertainty for the JYFLTRAP setup. The numbers were determined to be $\sigma_{\mathrm{m}}r/r = (7.8 \pm 0.3 \times 10^{-10}/u) \times \Delta m$ for the mass dependent and $\sigma_{\mathrm{res}}(r)/r = 1.2 \times 10^{-8}$. If the mass difference range was restricted to $\pm$24, the value for the mass dependent effect is found to be $\sigma_{\mathrm{m,lim}}(r)/r = (7.5 \pm 0.4 \times 10^{-10}/u) \times \Delta m$ and the corresponding residual uncertainty, $\sigma_{\mathrm{res,lim}}(r)/r = 7.9 \times 10^{-9}$. Justification for restricting to a narrower mass difference range is that the reference mass used at JYFLTRAP has never been further away than about 20 mass units from the ion of interest.

As shown in Fig. 3.20 for the data points where $m_{\mathrm{meas}} - m_{\mathrm{ref}}$ is -48 and +48, there is noticeable scatter in the results. This could be interpreted as an extra mass or frequency ratio related effect, but is in this case unlikely. Probably the reason for the scatter arises from the ion bunch preparation. The setup is optimised for a certain mass, thus with the same settings masses sufficiently heavier or lighter do not enter the precision trap in an optimal way. For example, in the case of C_{10} against C_6 two measurement sets were done. In addition to measuring on a different days, difference between the two sets includes different purification trap settings.

Still a decision remains should results on mass measurements be corrected with the obtained mass dependent effect or only add uncertainty. If the reference mass is relatively far away from the mass of interest probably then it is worthwile to correct with the effect. In the case of having only small mass difference it is maybe somewhat a matter of taste.

4 Yield measurements with light-ion induced reactions

4.1 Introduction

As mentioned in chapter 3, at IGISOL there are two methods to produce neutron-deficient isotopes. These are heavy-ion induced and light-ion induced fusion reactions. With the heavy-ion induced reactions the aim is to produce the most exotic isotopes. The less exotic ones are easier to produce with light-ion induced reactions. The primary beam intensity available from the K-130 cyclotron is considerably higher for light ions than for heavy ions, especially for protons. This can compensate the lower reaction cross sections for slightly more exotic isotopes. For example, for 30 MeV protons an intensity of several tens of microamperes can be achieved while for heavy ions typical intensities used at IGISOL are of the order of a few ten to a hundred particle nanoamperes. Additionally the population of different spin states is different with the complementary fusion reaction approaches. Heavy-ion induced reactions favor isomers with higher spin-states while light-ion induced reactions can populate all low-lying states.

To investigate the production of exotic isotopes with light-ion induced reactions two beam-time periods were partly dedicated for measuring the yields with the JYFLTRAP setup. The first period was conducted with a proton beam and the second with a ^{3}He beam, both with two different targets. The measurements presented in this work were concentrated in the region between strontium and tin. In this region the mass surface was rather modestly known at the time of these measurements. The same astrophysical motivations remain as with this whole thesis work. These measurements should help to plan future mass and collinear laser spectroscopy experiments by providing relative production cross sections.

The measurements described in this chapter were partly reported in Ref. [48] included in the appendix.

4.2 Measurement and analysis procedure

A collimated proton (62 MeV) or $^{3}He^{2+}$ (70 MeV) beam from the K-130 cyclotron was tuned to the light-ion ion guide. The targets used in these measurements were of a few mg/cm^2 thick 98% enriched ^{92}Mo, 66.4% enriched ^{106}Cd and natural ruthenium sputtered

on copper backing. The primary beam currents were1–1.3 μA for protons and 1.5–2.1 eμA for $^{3}He^{2+}$, respectively. The gas pressure in the ion guide was 150–200 mbar.

The ions were transported to the purification Penning trap for measurements. The ions were purified with either 500 ms or 350 ms isobaric purification cycles and extracted for counting on the Micro-Channel Plates (MCP). As shown in Fig. 3.12 the purification scan contains a few neighbouring isobars. The scan is repeated several times and the result shown in the figure is a sum of individual scans. The full-width at half-maximum of the peaks of the scans is about 20 Hz corresponding to a mass resolving power of $R = 6 \times 10^4$. A Gaussian fit was made to the data and from the peak maximum the detected yield was calculated.

In some cases the neighbouring elements in the same isobaric chain could not be distinguished because of their overlap therefore only a maximum yield could be determined. No efficiencies (MCP, transmission, etc.) were corrected for in the analysis assuming they are the same for all isotopes of the same element. By concentrating on isotopic chains the chemical effects could be excluded. More details on the measurement principle and the setup of the JYFLTRAP system are given in chapter 3.

In Ref. [48] (see Appendix) the proton induced yields were compared to Valeri Rubchenya's calculations. The model for the calculations is described in Ref. [49].

4.3 Results and discussion

4.3.1 General comments on the results

Here the obtained yield results are presented with comments on each graph. No efficiencies (MCP, transmission, chemistry, etc.) were taken into account in the analysis and therefore only relative yields for isotopic chains are reproduced. The half-lives of the measured isotopes were long compared to the trapping time. Therefore, no corrections for decay losses were needed. Fig. 4.1 shows an overview of which radioactive ions were detected using the Penning trap setup for purification.

A frequency resolution of about 20 Hz corresponds to an energy difference of about 2 MeV for mass $A = 100$. Thus the resolution is not enough to separate close-lying isomers from each other. Isomers are quite abundant in the nuclide chart region investigated and have half lives long enough to survive the measurement. Therefore, the detected yields are sums of the ground states and possible isomers. Near the valley of stability neighbouring isobars can overlap. This is often seen as a wider peak in the purification trap scans. In these cases it was possible to determine a maximum yield. The detected yields are shown in Figs. 4.2–4.5. The uncertainties in the data points are only statistical.

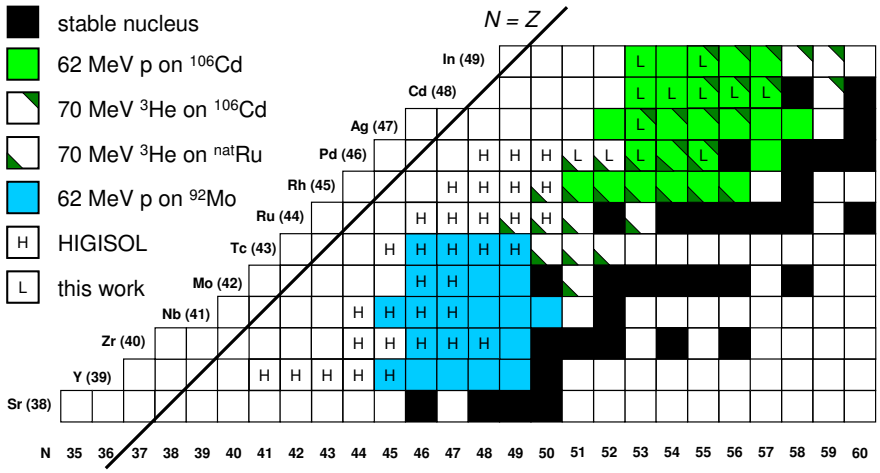

Fig. 4.1: Detected radioactive isotopes after isobaric purification produced in light-ion induced fusion evaporation reactions (coloured boxes). The masses measured in [11] and [50] produced in heavy-ion reactions are marked with "H". The mass of the isotopes marked with "L" are reported in [48]. ^{101}Cd was not visible in the performed purification trap scans. Still, the production rate was enough that the mass could be measured.

4.3.2 Detected yields

In Fig. 4.2 the target material was enriched ^{92}Mo and the projectile protons. All the isotopes were well separated from their isobars and thus the Gaussian fits could be used to extract the data shown in each subfigure. As an example, the niobium yields have been plotted with both statistical uncertainties as well as a conservative 30% uncertainty caused by beam fluctuations (see next subsection).

The primary beam in Fig. 4.3 was protons impinging on an enriched ^{106}Cd target. All the isotopes in the subfigure showing the detected indium yields were well separated. In the subfigure showing silver isotopes the neutron number $N = 57$, ^{104}Ag, could not be separated from the isobar of ^{104}Cd. Therefore the (maximum) yield has been given as the same for both isobars. All other silver isotopes were well separated from their isobars.

The Fig. 4.4 has three subfigures where the reaction was a ^{3}He beam impinging on an enriched ^{106}Cd target. The indium isotopes presented were all well separated from their isobars. In the subfigure of the cadmium isotopes, the yields of $N = 58$ and $N = 60$ might not only be due to the reaction, but also to sputtered target material. The target was enriched

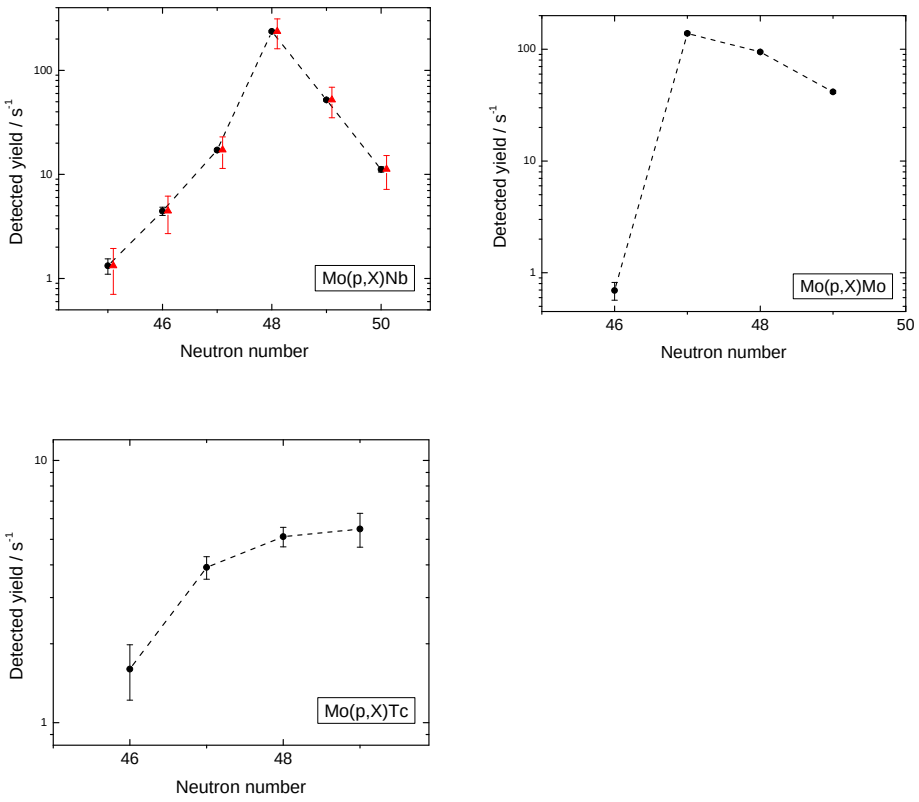

Fig. 4.2: Proton induced yields on molybdenum target. The niobium yields have been plotted both with statistical uncertainties (solid circles) and with a conservative 30% uncertainty (solid triangles) caused by the beam fluctuation (see text).

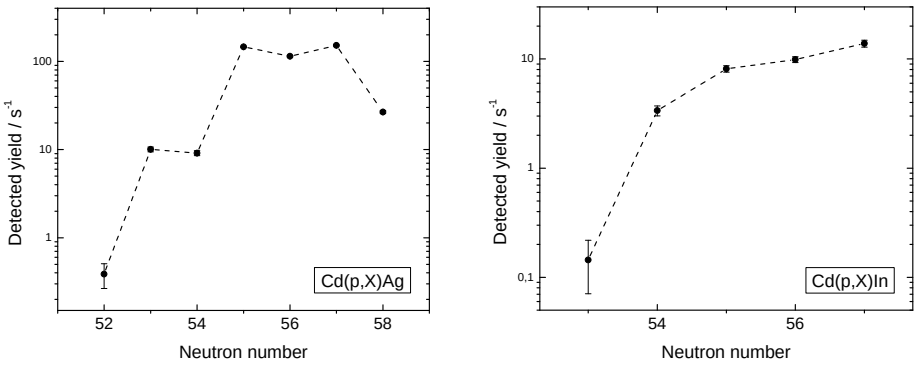

Fig. 4.3: Proton induced yields on cadmium target.

with 66.4% ^{106}Cd leaving an abundance for ^{108}Cd of only 0.62%. The ratio between the detected yields is about 0.15 instead of 0.01 expected from the target material. It should be noted that the MCP saturation limit was exceeded in the measurement of ^{106}Cd, resulting in an unreliable number for the actual yield of ^{106}Cd. The cadmium isotopes $N = 56$ and $N = 59$ can not be separated from their isobaric neighbours of ^{104}Ag and the stable silver isotope ^{107}Ag.

In Fig. 4.5 the target material was natural ruthenium and the projectile ^{3}He. The palladium isotope $N = 52$ was partly overlapping with a noticeably larger peak of ^{98}Rh but still a half Gaussian was possible to fit. The isotope ^{100}Pd can not be separated from ^{100}Rh. The resolving power was enough to partly reveal the palladium isotope $N = 55$ making it possible to fit half of a Gaussian curve. The peak is partially overlapping with the combined peak of ^{101}Rh and ^{101}Ru. The rhodium isotopes of $N = 54$ and $N = 56$ can not be separated from their ruthenium isobars which both are stable target material. It is possible that the target material was sputtered, which may have a big influence on the measured yields. Another stable ruthenium isotope is $N = 52$. The stable ruthenium isotopes are marked to the corresponding subfigure with red stars. The resolving power was not enough to separate ^{94}Ru and ^{94}Tc.

4.3.3 Converting detected yields into relative cross sections

In an ideal situation the beam would be stable, no chemical effects take place in the buffer gas volumes and no count rate or mass related effects take place anywhere in the system.

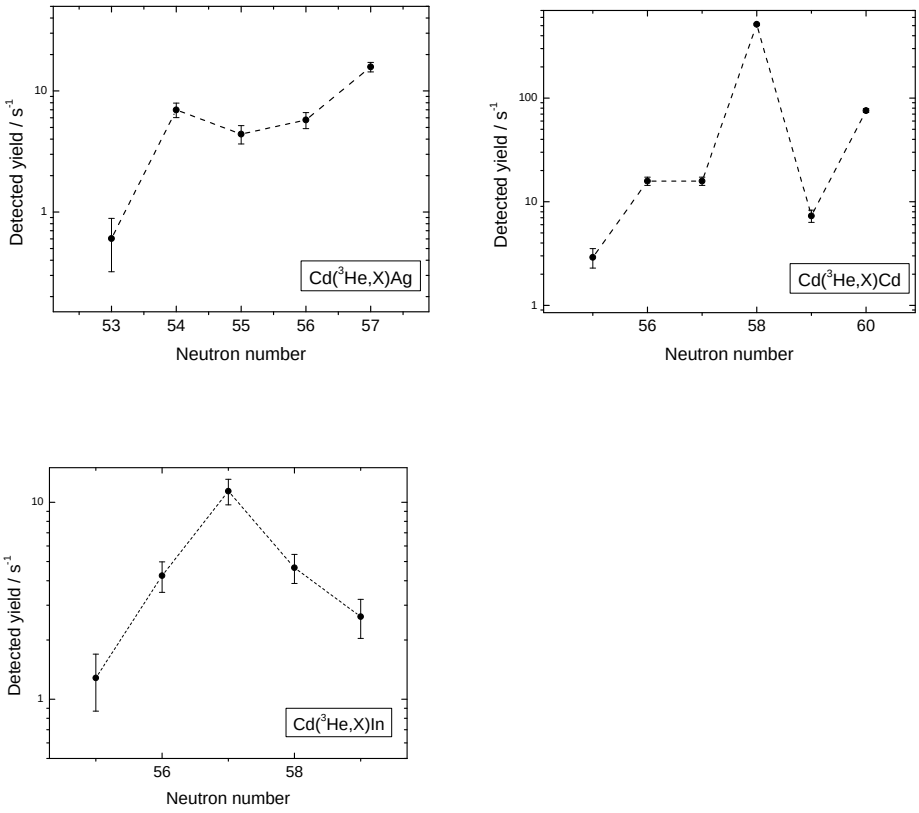

Fig. 4.4: Detected ^{3}He induced yields on an enriched cadmium target.

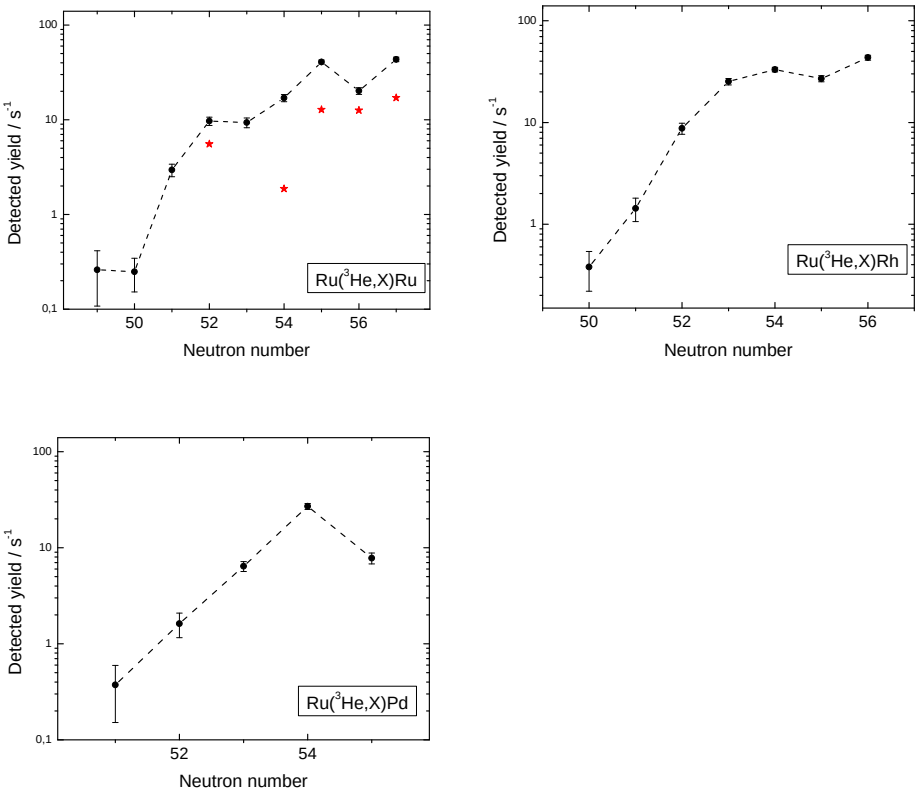

Fig. 4.5: Detected ^{3}He induced yields on ruthenium target (black filled circles). The red stars indicate the natural abundance of the stable ruthenium isotopes in the measurement region.

Then the detected yields could be directly converted into relative cross sections. Because this is not the case, these effects need to be estimated. One of the effects, for example, is caused by the detector limitations.

The ion bunch size is known to affect the detected yield in such a way that if the size is too large pile up takes place in the MCP. The maximum detection limit of the MCP is in the range of MHz. However in a bunched beam the ions can hit the detector in a fairly short time window. Typically the width is of the order of tens of μs. In practice, with the time-of-flight structure of this work the MCP starts to saturate when the bunch size exceeds about 100 ions.

In the majority of measurements reported here the saturation limit was not reached. Exceptions to this include ^{92}Mo which was part of the yield monitoring reference when the proton beam was impinging molybdenum target. Additionally, in the measurement of ^{106}Cd(^{3}He,X)^{106}Cd the limit was exceeded and the detected yield was about 185 ions per bunch. Because the reference measurement was made only to monitor the overall beam stability it is not a serious issue. The measured yield of ^{106}Cd is however not reliable.

Helium gas is used in three parts of the system for buffer gas purposes. These are the ion guide, the RFQ and the purification trap. It is obvious that some chemical effects take place in the ion guide and therefore the measured yields can only be interpreted as relative production yields within an element. As long as the purification cycle is kept constant the chemical effects of the trap system should cancel out.

To restrict the ion count rate the reaction product beam is pulsed before the RFQ. In this manner only part of the whole beam is allowed to be cooled and bunched before release to the purification trap. However, this has a side effect in that those isotopes that arrive earlier to the RFQ have more time to react with the buffer gas. If different pulse times are used, different isotopes can have different times spent in the RFQ. This was realised only well after the measurements in context were made with the analysis of fission production yields [51]. Fortunately the elements reported here are not particularly reactive or the pulsing times were varied little over the whole isotopic chain and thus effects should be far smaller than other uncertainties of this work.

By far the largest uncertainty is caused by the fluctuations seen in the count rate. Both short (even less than minute scale) and long (time scale of hours) term fluctuations are observed. In Figs. 4.6 and 4.7 the yield measurements performed with proton induced fission are shown as examples. Each individual point in the figures represents a sum over all the frequencies in one isobar scan. Reasons for the fluctuations can be instabilities in the primary beam or the electric or magnetic ion optical elements. The dipole magnet (mass separator) is thought to be the main source of the effects based on computer monitoring of the magnetic field used after these measurements.

It is possible to correct the long term drift in the detected yields by fitting a general trend to the reference scans. The short term fluctuations are more difficult to take into account. For

this the magnetic field would have to be constantly recorded, which was not possible at the time of the measurements. The maximum short term fluctuation over the mean value was between 10–20%. The effect of the long term drift on the isotope chains reported here is at maximum roughly 20%. Therefore a very conservative estimate for a yield uncertainty caused by the fluctuations is 30%.

During these measurements the cyclotron providing the primary beam sometimes had stability problems. The occasions can be seen in Figs. 4.6 and 4.7 as larger scatter at masses $A = 86, 90, 91$ and a few of the reference scans. Without the means to record the primary beam intensity fluctuations the effects are nearly impossible to correct. In the worst case the effect can be an order of magnitude. In Ref. [48] the niobium yields were compared to a theoretical cross section calculation. If the primary beam fluctuations are taken into account the true yield of the isotopes $N = 49, 50$ (mass numbers 90 and 91) would be higher. At these masses the yield trend would then be closer to that of the cross section calculations. When the primary beam was ^{3}He the mass $A = 94$ shows a count rate fluctuation which can be related to primary beam instabilities.

Partly because of limited measurement time and partly due to a lack of experience the measurements were not done in an ideal manner. Nevertheless, the results give confidence that the JYFLTRAP setup can be used to investigate relative reaction cross sections with reasonable accuracy provided that some improvements to the setup are made. Since these measurements the dipole magnet field is monitored and can be saved for later analysis. The magnet control has been transferred from manual to automatic noticeably increasing stability. Furthermore, the online monitoring of the measurement has since been installed making it possible to remeasure isotopes within a short time. The recording of the primary beam intensity is still missing. For the moment it is only monitored from a Faraday cup readout by the weary eyes of whosoever is on duty.

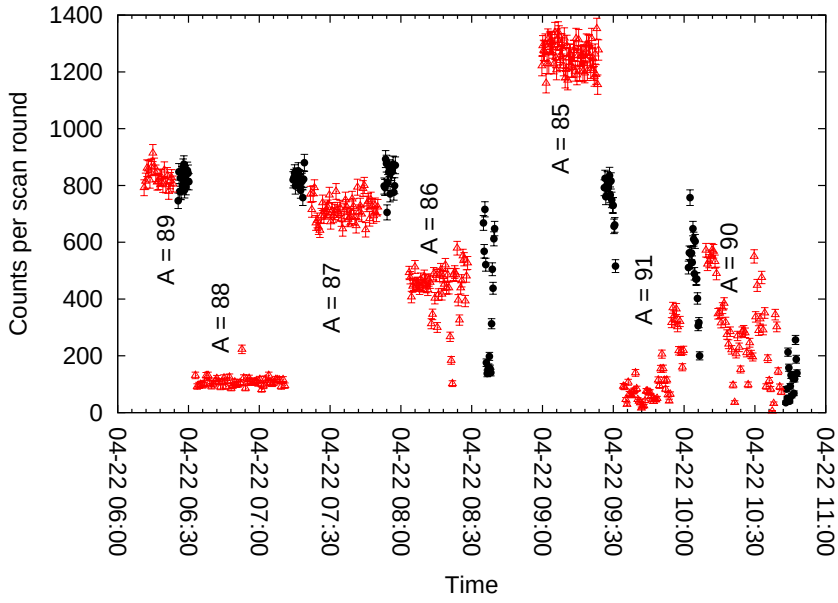

Fig. 4.6: Detected total counts in one scan round. The primary beam was protons impinging on a molybdenum target. Each individual point represents a sum over all the frequencies in the whole isobar scan. The beam stability reference was $A = 92$, black circles. The measurements are drawn with red triangles and the mass number is indicated.

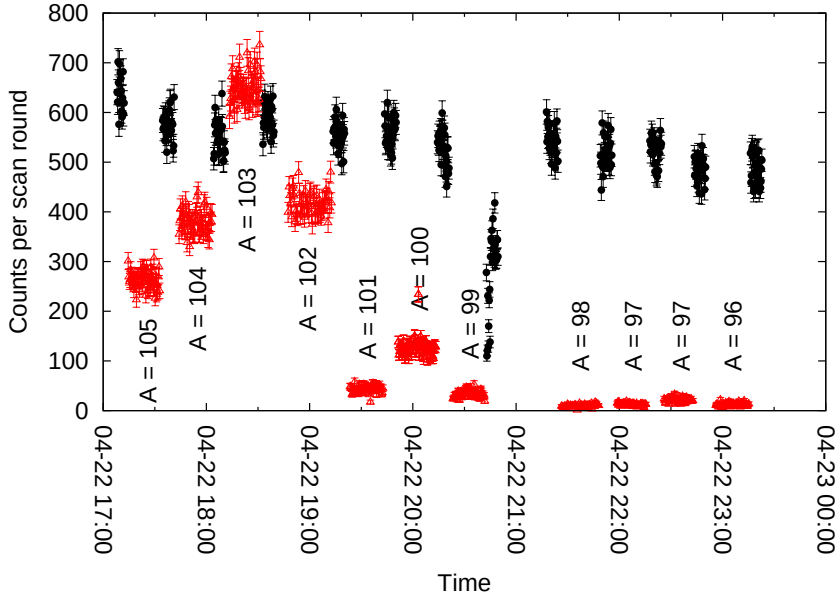

Fig. 4.7: Detected total counts in one scan round. The primary beam was protons impinging on a cadmium target. Each individual point represents a sum over all the frequencies in the whole isobar scan. The beam stability reference was $A = 106$, black circles. The measurements are drawn with red triangles and the mass number is indicated.

5 Mass measurements in the region of the rp process

5.1 Measurement procedure and results

Masses relevant to the rp and νp processes studied in this work were measured during five on-line measurement periods. Two of these were dedicated to light-ion induced fusion evaporation reactions and the rest for heavy-ion induced fusion reactions. Part of the work was performed in collaboration with the SHIPTRAP group from GSI, Darmstadt, see Ref. [11].

In light-ion fusion evaporation reactions the targets used were ^{nat}Ru and 66.4% enriched ^{106}Cd. The primary beams were 62 MeV protons and 70 MeV or 100 MeV ^{3}He, respectively. In heavy-ion induced fusion reactions, ^{36}Ar, ^{40}Ca or ^{58}Ni beams were used at several different energies of the order of $4 - 6$ MeV per nucleon. The target in each heavy-ion experiment was ^{nat}Ni of 4 mg/cm^2 thickness. The produced ions of interest were transported to the Penning trap system in a standard way and the conventional excitation scheme was used in the TOF-ICR measurements. ^{85}Rb^{+} and ^{94,96,97}Mo^{+} were used as the reference ions. See the publications of this work for more details on the measurement settings.

All results are summarised in three tables in appendix A. Those measurements that were done in collaboration with SHIPTRAP have been averaged. For some of the measurements a different reference mass was used. In those cases a weighted average was taken from the mass excesses only. When the same reference mass was used, the weighted average of the frequency ratios was calculated and a common mass excess was determined.

5.2 Discussion

5.2.1 General comments on results

A large number of the masses measured in this work were experimentally determined for the first time. In particular, the masses of isotopes which were produced by heavy-ion induced reactions improved the information of the mass surface in the region of tin and below. Comparison to the previous measurements and to the mass evaluation values of [52] has been made in Ref. [11]. Because of limited space of the Physical Review Letters, the literature values are only listed in Ref. [53]. In the technetium isotopes a large deviation to the previous values can be seen. The mass of ^{88}Tc deviates as much as 1 MeV compared to

the extrapolation of [52]. Other measurements are mostly in agreement with the literature values but the uncertainties have been improved satisfying nuclear astrophysics calculation needs.

Masses for radioactive isotopes of $^{97-99,101}$Pd, ^{100}Ag, $^{101-104}$Cd and ^{102,104}In were determined by using light-ion induced fusion evaporation reactions to produce the ions. None of the determined masses was a new measurement but the information has been improved as can be seen from the comparison to the literature values [48]. A few of these masses were measured by the SHIPTRAP group, reported in [54]. A noticeable deviation was observed for some of the cadmium isotopes between JYFLTRAP and SHIPTRAP. The reason for this still remains unresolved. The ISOLTRAP group at CERN [31] has since measured the same masses however the results have yet to be published.

The isotopes measured in this work cover a good portion of the regions of the rp- and νp-process paths above molybdenum. Some work remains still in order to probe deeper to the paths themselves. An exception is the proposed endpoint region of the rp process in the tin-antimony region which is now well covered by the new mass measurements.

5.2.2 Astrophysics aspects

In astrophysics, an often used model for obtaining atomic masses is the Finite-Range Droplet Model (FRDM) [14]. Figs. 5.1 and 5.2 illustrate the difference between the mass excesses obtained in this work and the literature values of AME2003 [52] and those calculated with the FRDM for two elements: palladium and antimony. The experimental values of JYFLTRAP agree well with those of Ref. [52], partly because most of the previous values have large uncertainties. The values given by the FRDM calculation seem to scatter around the experimental ones by several hundred keV.

The mass of an atom is an important quantity. For astrophysical modelling even more so is the proton separation energy (see section 2.3). Figs. 5.3–5.7 show comparisons for the proton separation energies calculated with the FRDM [55] and those obtained in this work and AME2003 [52]. Proton separation energies for tellurim, antimony and tin isotopes are calculated in Ref. [53]. The S_p values for rhodium and palladium isotopes are calculated from the masses reported in Refs. [11] and [48] by taking the masses for $^{96-98,100}$Rh and ^{1}H from [52]. As can be seen in the figures the trends of the proton separation energies of FRDM are reproduced better than the masses. However, the values can still differ by several hundred keV. In the case of antimony the isotopes ^{106}Sb and ^{107}Sb are predicted to be proton unbound. The values evaluated in [52] agree well with this work but again because their large uncertainties.

Note that in Fig. 5.7 the proton separation energy of ^{107}Te is calculated using its extrapolated mass excess of -60540#(300#) from AME2003 [52]. The proton separation energy of ^{106}Te has been derived using its mass excess of -58210(130) from AME2003, the ^{104}Sn mass from

this work and $Q_p(^{105}\mathrm{Sb})$ from [56]. An improved mass excess for ^{106}Te can be calculated using the masses from this work:

$$ME(^{106}\mathrm{Te}) = ME(^{102}\mathrm{Sn}) + M(^{4}\mathrm{He}) + Q_\alpha(^{106}\mathrm{Te}) = -58200(70)keV, \quad (5.1)$$

where

$$ME(^{102}\mathrm{Sn}) = ME(^{102}\mathrm{In}) + Q_{\beta^-}(^{102}\mathrm{Sn}). \quad (5.2)$$

Here the decay energies are from [57], the mass of ^{4}He from [52] and the mass excess for ^{102}In has been reported in [48]. The final uncertainty is governed by the uncertainty of the β decay of ^{102}Sn which has a Q value of 5780(70) keV. The mass excess for ^{106}Te in [52] is $-58210(130)$ keV. Therefore the actual mass excess has barely changed but the uncertainty is almost halved. If this value would be implemented in the proton separation energy of ^{106}Te in Fig. 5.7 the value would not shift much but the uncertainty would be reduced by almost a factor of two.

Masses of n-deficient isotopes measured in the present work along with the values from AME2003 and Ref. [50] were used in the νp-process nucleosynthesis calculations. The calculations were performed to find out the effect of the new mass values on the reaction flow and final abundances. The main motivation was to find out if the abundances of light isotopes of molybdenum and ruthenium would change using th new mass information. An accurate description of the calculation methods and results are given in Ref. [11]. In summary, the reaction flow around ^{88}Tc is modified compared to the calculations done with masses only from AME2003. The main reason for this is the 1 MeV difference in proton-separation energy of ^{88}Tc calculated from the new masses. The final abundances for the νp process did not change noticeably.

The rp process has been modelled to end in a closed SnSbTe cycle, see Ref. [5]. The proton separation values from Refs. [56] and [52] for ^{104}Sb and ^{105}Sb already prevented those nuclides to be used as a channel to a closed cycle. The only channel left for the tellurium nuclides was via ^{106}Sb. A previous measurement of $S_p(^{106}\mathrm{Sb}) = 930(210)$ keV [58] still allowed a reasonable branching into the SnSbTe cycle. The direct mass measurement of ^{106}Sb at JYFLTRAP gave a new value of $S_p = 424(8)$ keV. This value clearly differs from the old measurement and is the main reason for diluting the possibility for a closed SnSbTe cycle. In conclusion, the rp process will have to move closer to the line of stability before a closed loop is formed.

The reaction rate – Eq. (2.2) – not only depends on the masses of the isotopes involved but also on the resonance strength. That again is sensitive to the spins and parities. So far much of the rp- and νp-process calculations in the endpoint region of the process have depended only on the ground-state information. It is possible that the isomeric states play a larger role on the nucleosynthesis paths than so far taken into account. The problem is that the spins and parities of the isomeric states, and often the ground states also, are scarcely known. In addition, the excitation energies are also incorrectly known. Therefore, these aspects should be investigated more closely.

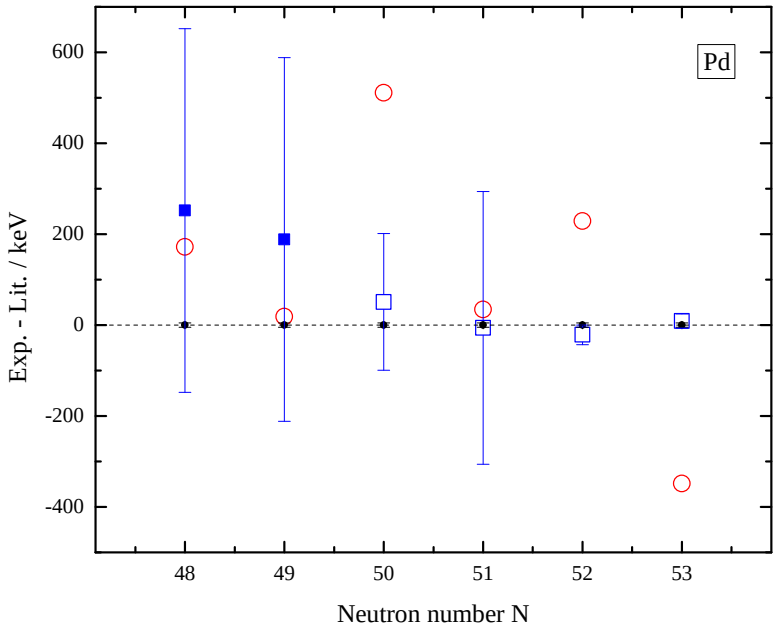

Fig. 5.1: Comparison of mass excesses of palladium isotopes from this work (black points) to the literature values of AME2003 [52] (blue squares) and to FRDM values [14] (red open circles). The filled blue squares indicate those literature values which are based on extrapolations of systematic trends.

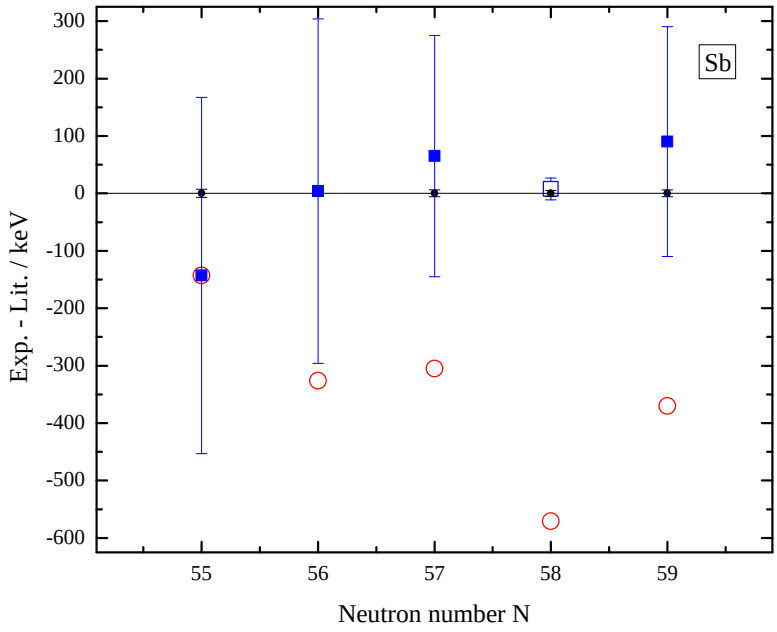

Fig. 5.2: Comparison of mass excesses of antimony isotopes from this work (black points) to the literature values of AME2003 [52] (blue squares) and to FRDM values [14] (red open circles). The filled blue squares indicate those literature values which are based on extrapolations of systematic trends.

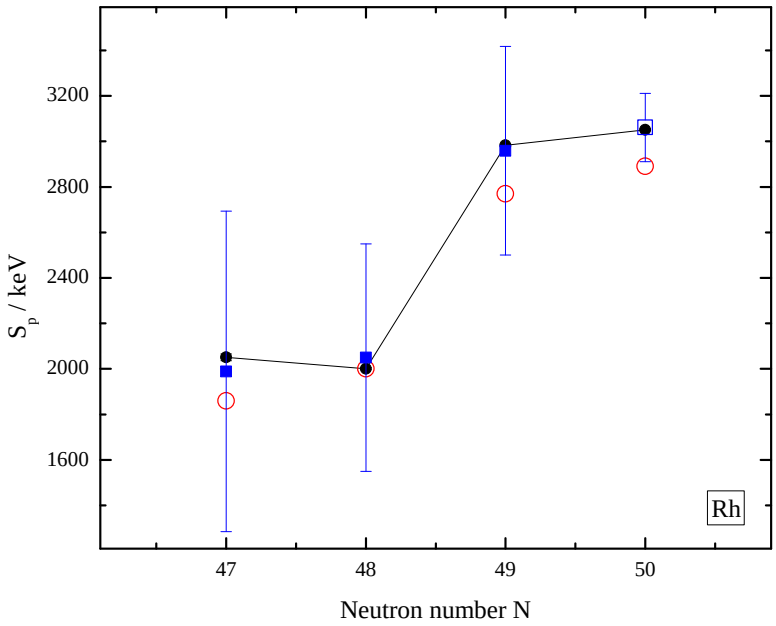

Fig. 5.3: Comparison of the proton separation energies of rhodium isotopes (black points) from this work to FRDM values (red open circles) from Ref. [55] and to the AME2003 values [52] (blue squares). The filled blue squares indicate those AME2003 values which are based on extrapolations of systematic trends.

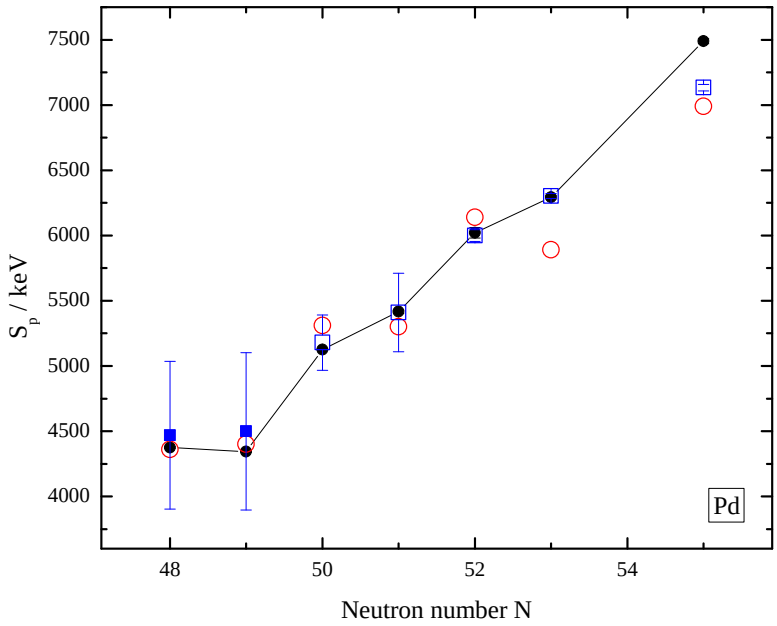

Fig. 5.4: Comparison of the proton separation energies of palladium isotopes (black points) from this work to FRDM values (red open circles) from Ref. [55] and to the AME2003 values [52] (blue squares). The filled blue squares indicate those AME2003 values which are based on extrapolations of systematic trends.

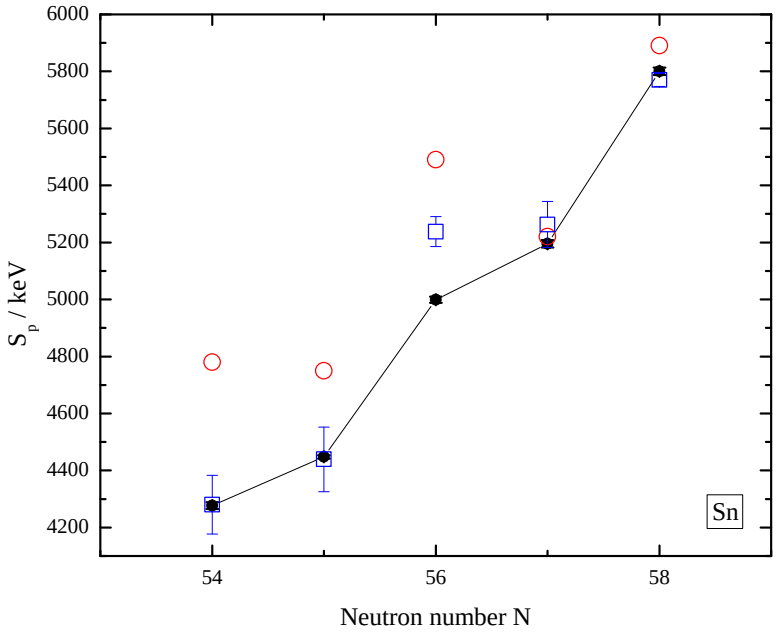

Fig. 5.5: Comparison of the proton separation energies of tin isotopes (black points) from this work to FRDM values (red open circles) from Ref. [55] and to the AME2003 values [52] (blue squares).

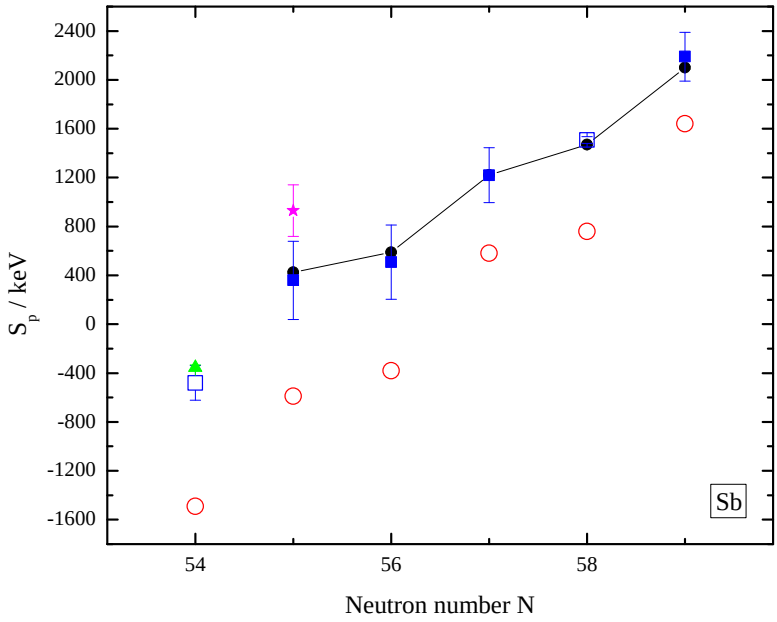

Fig. 5.6: Comparison of the proton separation energies of antimony isotopes (black points) from this work to FRDM values (red open circles) from Ref. [55] and to the AME2003 [52] (blue squares). The green triangle for ^{105}Sb of -356(22) keV is from Ref. [56]. The pink star for ^{106}Sb of 930(210) keV [58] was disgarded from the AME2003 evaluation. Nevertheless, it has been used in endpoint calculations (see Ref. [53] and references therein). The filled blue squares indicate those AME2003 values which are based on extrapolations of systematic trends.

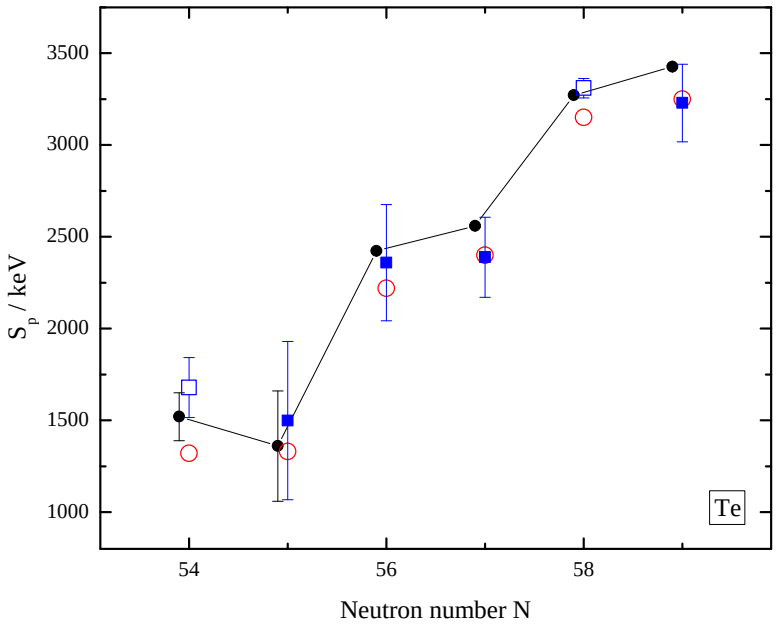

Fig. 5.7: Comparison of the proton separation energies of tellurium isotopes (black points) from this work to FRDM values (red open circles) from Ref. [55] and to the AME2003 values [52] (blue squares). Note that the proton separation value for ^{107}Te is calculated using its extrapolated mass excess from AME2003. The proton separation energy of ^{106}Te has been derived by using its mass from AME2003, the ^{104}Sn mass from this work and $Q_p(^{105}\mathrm{Sb})$ from [56]. To clarify the data the experimental points have been slightly shifted. The filled blue squares indicate those AME2003 values which are based on extrapolations of systematic trends.

5.2.3 The case of ^{94m}Ag

From the heavy-ion induced fusion reaction mass measurements rose an interesting spin-off, the case of ^{94}Ag and most importantly the high-spin isomer (21+). Motivation for the studies of ^{94m}Ag are not the relevance to nucleosynthesis but rather its exotic decay properties. The silver isomer can decay via several different paths, for example β-delayed proton decay or via direct one- or two-proton decay modes. To study ^{94}Ag along with its isomer the masses involved should be experimentally determined.

Although the mass of ^{94}Ag or the isomer were not directly measured in this work, the mass of close-lying ^{92}Rh and ^{94}Pd were determined. ^{92}Rh is the two-proton decay daughter and ^{94}Pd is the β-decay daughter of ^{94}Ag. From the mass of ^{94}Pd the Q_{EC} value of ^{94}Ag can be relatively well determined from the Coulomb displacement energy. Then from the Q_{EC} the mass of ^{94}Ag can be obtained with the knowledge of the mass of ^{94}Pd. The detailed calculation is presented in [59]. A mass excess for ^{94}Ag has been determined to be $-53\,330(360)$ keV. From this and the mass of ^{92}Rh a two-proton separation energy can be obtained, $S_{2p} = 4910(360)$ keV. In Ref. [60] the two-proton decay of ^{94m}Ag (21+) was studied. By combining the information from Mukha *et al.* with information for ^{92}Rh [61], the excitation energy and mass excess for ^{94m}Ag (21+) can be determined to be $E_x = 8360(370)$ keV and $\Delta = -44\,970(100)$ keV, respectively.

Another way to extract the ^{94m}Ag (21+) excitation energy is via the one-proton decay daughter ^{93}Pd. The mass of ^{93}Pd was obtained from an interpolation of the two-proton separation energies in the $N = 47$ isotopes. Finally, a mass excess and an excitation energy for ^{94m}Ag (21+) can be obtained by combining the mass of ^{93}Pd, the proton-separation energy of ^{93}Pd (the mass for the proton decay daughter ^{92}Rh was measured both at JYFLTRAP and SHIPTRAP) and one-proton decay data from Ref. [62]. The obtained value for ^{94m}Ag (21+) excitation energy is 6960(400) keV and the mass excess $-46\,370(170)$ keV.

The values obtained via the two approaches above for the (21+) isomer of ^{94}Ag do not agree with each other. Possible explanations for the discrepancy are given in [59]. It might be that some γ transitions were not observed in the one-proton decay data because of a large background created by the β-delayed γ rays. Then the isomeric energy could lie around 8.4 MeV instead of ~ 7 MeV.

Another isomeric anomaly studied at JYFLTRAP is ^{95}Pd. The mass of both the $9/2^+$ (extrapolated spin and parity) ground state and the isomeric state with uncertain spin and parity of $21/2^+$ were directly determined. The mass excesses were -69961.6(4.8) for the ground state and -68086.2(4.7) for the isomeric state. Therefore the excitation energy is 1875(7) keV while the extrapolated excitation energy in AME2003 is 1860#(500#).

6 Summary and outlook

Almost 50 masses of neutron-deficient isotopes in the region of tin and below were measured. The masses are crucial for the nucleosynthesis model calculations. The rp process has been proposed to end in the so-called SnSbTe cycle [5]. The new results no longer allow a strong cycle to be formed. Most of the new masses were also used in νp-model calculations to find out if they would solve the mystery of fairly abundant, stable, light molybdenum and ruthenium isotopes. No conclusive result was found.

To probe deeper into the rp process path some ion guide development is required. For the moment the efficiency of the heavy-ion guide is rather low, only fractions of a percent. One way to increase the efficiency is to use a laser-ion source. In this method the reaction products are produced in a conventional manner but instead of directly extracting them out from the ion guide they are allowed to neutralise. When all the ions are neutral they are selectively ionised depending on the element. The dipole magnet provides the isotopic purification and the outcome is one isotope of one element. For this purpose the FURIOS program was launched a few years ago and is steadily progressing towards laser online ions. The hope is that the efficiency of the ion guide would even increase a hundred-fold from the present. Until the laser-ion guide is ready to roll, the mass measurements relevant for the rp process are continuing in slightly less exotic regions of the nuclide chart.

To investigate the systematic effects of the JYFLTRAP setup a carbon-cluster ion source was built. The source was used to determine the mass-dependent effect and the residual uncertainty of the system. Two sets of values were extracted for both effects. If all the measurements were analysed as one bulk the obtained values are $\sigma_{\mathrm{m}}r/r = (7.8 \pm 0.3 \times 10^{-10}/u) \times \Delta m$ for mass dependence and $\sigma_{\mathrm{res}}(r)/r = 1.2 \times 10^{-8}$ for the residual uncertainty. If the mass difference between the reference ion and ion of interest is restricted to ± 24, the values are $\sigma_{\mathrm{m,lim}}(r)/r = (7.5 \pm 0.4 \times 10^{-10}/u) \times \Delta m$ and $\sigma_{\mathrm{res,lim}}(r)/r = 7.9 \times 10^{-9}$.

In the coming year or so the whole IGISOL setup will move to a new accelerator hall and at this time the Penning trap magnet has to be shut down. All the systematic measurements have to be at least partly redone to confirm the trap performance after re-energising the magnet.

Plans include the construction of a dedicated off-line ion source station which would also house the carbon-cluster ion source. It would be highly useful if it can be built such that the power of the dipole magnet can be exploited and also so that the ions from the source could be switched between the IGISOL ions in the blink of an eye. So far no one has routinely used the carbon clusters as reference ions for mass measurements. With a separate off-line

ion station this could be realised easier than at present. Also, if the carbon-cluster ion source is built to a separate high-voltage platform it would be possible to circumvent the occasional sparking problems it now has with the high voltage.

The JYFLTRAP setup was used to investigate relative light-ion induced fusion yields. The measured proton-induced relative yields were compared to a statistical model calculation. The tests proved succesful despite the minor stumbles taking place on the way. For example, the significance of the dipole magnet fluctuations was not realised until after the measurements, at the time of data analysis. Computer control installed thereafter has helped to stabilise the magnet. It still remains to be seen if the stabilisation effect is enough for getting more precise and hopefully also more accurate relative yield measurements. Another notable upgrade has been the online monitoring of the JYFLTRAP measurements.

A Mass excesses

In this appendix all the masses measured in this work are summarised in three tables. Some of the masses were measured both at JYFLTRAP and SHIPTRAP at GSI. An average mass excess was quantified from an average frequency ratio when applicable, otherwise it was averaged from the mass excesses acquired at both facilities. All the values are listed.

Table A.1: Measured frequency ratios r and derived mass excess values (ME) using the reference mass values from [52].

Nuclide	Reference	$r = \nu_{\mathrm{c,ref}}/\nu_{\mathrm{c}}$	ME (keV)	Note
^{84}Y	^{97}Mo	1.031056762(53)	-73888.8(5.2)	$\star$,†
^{87}Zr	^{97}Mo	1.061954361(54)	-79341.4(5.3)	$\star$
^{88}Mo	^{85}Rb	1.035450878(48)	-72686.5(3.8)	
^{89}Mo	^{85}Rb	1.047198443(49)	-75015.0(3.9)	
^{88}Tc	^{85}Rb	1.035590047(48)	-61679.1(3.8)	‡, #
^{89}Tc	^{85}Rb	1.047294785(48)		JYFLTRAP, #
^{89}Tc	^{85}Rb	1.047294809(203)		SHIPTRAP, #
^{89}Tc	^{85}Rb	1.047294786(47)	-67394.8(3.7)	Ave., #
^{90}Tc	^{85}Rb	1.059029703(49)		JYFLTRAP
^{90}Tc	^{85}Rb	1.059029697(94)		SHIPTRAP
^{90}Tc	^{85}Rb	1.059029702(43)	-70723.7(3.4)	Ave.
^{91}Tc	^{94}Mo	0.968194724(47)	-75983.4(4.5)	JYFLTRAP
^{91}Tc	^{85}Rb	1.070740167(63)	-75986.5(5.0)	SHIPTRAP
^{91}Tc			-75984.8(3.3)	Ave.
^{92}Tc	^{85}Rb	1.082480001(50)		JYFLTRAP
^{92}Tc	^{85}Rb	1.082480188(137)		SHIPTRAP
^{92}Tc	^{85}Rb	1.082480023(47)	-78924.7(3.7)	Ave.

$\star$ The frequency ratio for an oxide was measured.
† Mass excess modified with a treatment for an unknown mixture of isomers [57] is -73922(19) keV.
‡ In Ref. [11] the original error of 3.8 keV is increased to 87 keV because of the unknown level scheme of isomeric states.
# The previous value [52] only estimated from systematic experimental trends.

Table A.2: Measured frequency ratios r and derived mass excess values (ME) using the reference mass values from [52].

Nuclide	Reference	$r = \nu_{c,ref}/\nu_c$	ME (keV)	Note
^{90}Ru	^{85}Rb	1.059103508(55)		JYFLTRAP, #
^{90}Ru	^{85}Rb	1.059103727(127)		SHIPTRAP, #
^{90}Ru	^{85}Rb	1.059103543(50)	-64883.3(4.0)	Ave., #
^{91}Ru	^{85}Rb	1.070838119(49)	-68239.1(3.9)	JYFLTRAP, #
^{91}Ru	^{94}Mo	0.968283302(50)	-68235.3(4.7)	JYFLTRAP, #
^{91}Ru	^{85}Rb	1.070838208(131)	-68232.0(10.4)	SHIPTRAP, #
^{91}Ru			-68237.1(2.9)	Ave., #
^{92}Ru	^{85}Rb	1.082538479(51)		JYFLTRAP, #
^{92}Ru	^{85}Rb	1.082538554(67)		SHIPTRAP, #
^{92}Ru	^{85}Rb	1.082538507(41)	-74299.0(3.2)	Ave., #
^{93}Ru	^{85}Rb	1.094278655(51)	-77214.0(4.0)	
^{94}Ru	^{85}Rb	1.105987814(53)		JYFLTRAP
^{94}Ru	^{85}Rb	1.105987624(289)		SHIPTRAP
^{94}Ru	^{85}Rb	1.105987808(52)	-82580.6(4.1)	Ave.
^{92}Rh	^{85}Rb	1.082681373(55)		JYFLTRAP, #
^{92}Rh	^{85}Rb	1.082681725(434)		SHIPTRAP, #
^{92}Rh	^{85}Rb	1.082681379(55)	-62999.1(4.3)	$\star$, Ave., #
^{93}Rh	^{85}Rb	1.094382341(53)		JYFLTRAP, #
^{93}Rh	^{85}Rb	1.094382514(141)		SHIPTRAP, #
^{93}Rh	^{85}Rb	1.094382362(50)	-69011.3(3.9)	Ave., #
^{94}Rh	^{85}Rb	1.106110107(54)	-72907.5(4.2)	#
^{95}Rh	^{85}Rb	1.117818397(53)	-78342.3(4.2)	
^{94}Pd	^{94}Mo	1.000255075(49)	-66097.9(4.7)	#
^{95}Pd	^{94}Mo	1.010860017(50)	-69961.6(4.8)	#
^{95}Pd^{m}	^{94}Mo	1.010881456(48)	-68086.2(4.7)	
^{96}Pd	^{94}Mo	1.021438050(48)	-76179.0(4.7)	
^{97}Pd	^{85}Rb	1.141379187(21)	-77805.9(4.9)	†
^{98}Pd	^{85}Rb	1.153111745(18)	-81321.3(4.8)	†
^{99}Pd	^{96}Mo	1.0313552482(83)	-82178.9(5.1)	†
^{101}Pd	^{96}Mo	1.0521730471(79)	-85427.1(5.2)	†

† The mass excess uncertainty has an estimated $5{\cdot}10^{-8}$ residual uncertainty included (see Ref. [11]) whereas the uncertainty of the frequency ratio does not.
$\star$ In Ref. [11] the original error of 4.3 keV is increased to 15 keV because of the unknown level scheme of isomeric states.
The previous value [52] only estimated from systematic experimental trends.

Table A.3: Measured frequency ratios r and derived mass excess values (ME) using the reference mass values from [52].

Nuclide	Reference	$r = \nu_{c,ref}/\nu_c$	ME (keV)	Note
^{100}Ag	^{85}Rb	1.176706087(18)	-78131.0(4.9)	⋆,†
^{101}Cd	^{96}Mo	1.052280501(23)	-75827.8(5.6)	†
^{102}Cd	^{96}Mo	1.0626647323(94)	-79655.6(5.3)	†
^{103}Cd	^{96}Mo	1.0730806977(90)	-80648.5(5.3)	†
^{104}Cd	^{96}Mo	1.083470676(19)	-83962.9(5.6)	†
^{105}Cd	^{96}Mo	1.093893644(11)	-84330.1(5.5)	†
^{102}In	^{96}Mo	1.062765089(15)	-70690.4(5.4)	†
^{104}In	^{85}Rb	1.223838813(20)	-76176.5(5.1)	†,‡
^{104}Sn	^{87}Rb	1.195767977(74)	-71625(6)	
^{105}Sn	^{87}Rb	1.207253180(64)	-73336(5)	
^{106}Sn	^{87}Rb	1.218709913(87)	-77351(7)	
^{107}Sn	^{87}Rb	1.230201911(65)	-78512(5)	
^{108}Sn	^{87}Rb	1.241664284(68)	-82071(6)	
^{106}Sb	^{87}Rb	1.218844285(92)	-66473(7)	#
^{107}Sb	^{87}Rb	1.230299077(67)	-70646(5)	#
^{108}Sb	^{87}Rb	1.241783189(68)	-72445(6)	#
^{109}Sb	^{87}Rb	1.253242516(68)	-76251(5)	
^{110}Sb	^{87}Rb	1.264734046(73)	-77450(6)	#
^{106}Te			-58195(71)	⋆⋆
^{108}Te	^{87}Rb	1.241865478(69)	-65784(6)	
^{109}Te	^{87}Rb	1.253347956(73)	-67715(6)	
^{111}I	^{87}Rb	1.276394688(70)	-64958(6)	#

† The mass excess uncertainty has an estimated $5{\cdot}10^{-8}$ residual uncertainty included (see Ref. [11]) whereas the uncertainty of the frequency ratio does not.
⋆ Mass excess modified with a treatment for an unknown mixture of isomers [57] is -78139(7) keV.
‡ Mass excess modified with a treatment for an unknown mixture of isomers [57] is -76223(28) keV.
⋆⋆ The mass excess is calculated from the α-decay energy of ^{106}Te [57] and the mass excess of ^{102}Sn, which is derived from the mass excess of ^{102}In [48] and the β-decay energy of ^{102}Sn [57].
The previous value [52] only estimated from systematic experimental trends.

Bibliography

[1] U. Hager, Ph.D. thesis, University of Jyväskylä, 2007.

[2] T. Eronen, Ph.D. thesis, University of Jyväskylä, 2008.

[3] A. Kankainen, Ph.D. thesis, University of Jyväskylä, 2006.

[4] F. Hoyle, Ap. J. Suppl. **1**, 121 (1954).

[5] H. Schatz *et al.*, Phys. Rev. Lett. **86**, 3471 (2001).

[6] Q. Z. Liu, J. van Paradijs, and E. P. J. van den Heuvel, Astron. Astrophys. **469**, 807 (2007).

[7] S. Migliari *et al.*, Mon. Not. R. Astron. Soc. **342**, 909 (2003).

[8] H. Schatz, Nucl. Phys. A **787**, 299c (2007).

[9] S. E. Woosley *et al.*, Ap. J. Suppl. **151**, 75 (2004).

[10] C. Fröhlich *et al.*, Phys. Rev. Lett. **96**, 142502 (2006).

[11] C. Weber *et al.*, Phys. Rev. C **78**, 054310 (2008).

[12] H. Schatz, Int. J. Mass Spectrom. **251**, 293 (2006).

[13] A. Wöhr *et al.*, Nucl. Phys. A **742**, 349 (2004).

[14] P. Möller, J. Nix, W. Myers, and W. Swiatecki, At. Data Nucl. Data Tables **59**, 185 (1995).

[15] D. Lunney, J. Pearson, and C. Thibault, Rev. Mod. Phys. **75**, 1021 (2003).

[16] M. Matos *et al.*, J. Phys. G: Nucl. Phys. **35**, 014045 (2008).

[17] B. Jurado *et al.*, Physics Letters B **649**, 43 (2007).

[18] A. S. Lalleman *et al.*, Hyp. Int. **132**, 315 (2001).

[19] Y. Ishida *et al.*, Nucl. Instrum. Methods Phys. Res., Sect. B **219-220**, 468 (2004).

[20] A. Piechaczek *et al.*, Nucl. Instrum. Methods Phys. Res., Sect. B **266**, 4510 (2008).

[21] W. R. Plaß *et al.*, Nucl. Instrum. Methods Phys. Res., Sect. B **266**, 4560 (2008).

[22] Y. Litvinov *et al.*, Nucl. Phys. A **756**, 3 (2005).

[23] S. Nagy *et al.*, Eur. Phys. J. D **39**, 1 (2006).

[24] W. Shi, M. Redshaw, and E. G. Myers, Phys. Rev. A **72**, 022510 (2005).

[25] A. Kellerbauer *et al.*, Eur. Phys. J. D **22**, 53 (2003).

[26] A. Chaudhuri *et al.*, Eur. Phys. J. D **45**, 47 (2007).

[27] P. Karvonen *et al.*, Nucl. Instrum. Methods Phys. Res., Sect. B **266**, 4794 (2008).

[28] A. Nieminen *et al.*, Nucl. Instrum. Methods Phys. Res., Sect. A **469**, 244 (2001).

[29] G. Savard *et al.*, Phys. Lett. A **158**, 247 (1991).

[30] G. Gräff, H. Kalinowsky, and J. Traut, Z. Phys. A **297**, 35 (1980).

[31] M. Mukherjee *et al.*, Eur. Phys. J. A **35**, 1 (2008).

[32] I. Bergström *et al.*, Nucl. Instrum. Methods Phys. Res., Sect. A **487**, 618 (2002).

[33] L. S. Brown and G. Gabrielse, Phys. Rev. A **25**, 2423 (1982).

[34] G. Gabrielse, Phys. Rev. Lett. **102**, 172501 (2009).

[35] G. Gabrielse, Int. J. Mass Spectrom. **279**, 107 (2009).

[36] T. Eronen *et al.*, Nucl. Instrum. Methods Phys. Res., Sect. B **266**, 4527 (2008).

[37] T. Eronen *et al.*, Phys. Rev. Lett. **100**, 132502 (2008).

[38] M. König *et al.*, Int. J. Mass Spectrom. Ion Processes **142**, 95 (1995).

[39] S. George *et al.*, Int. J. Mass Spectrom. **264**, 110 (2007).

[40] M. Kretzschmar, Int. J. Mass Spectrom. **264**, 122 (2007).

[41] S. George *et al.*, Phys. Rev. Lett. **98**, 162501 (2007).

[42] R. T. Birge, Phys. Rev. **40**, 207 (1932).

[43] G. Bollen *et al.*, Nucl. Instrum. Methods Phys. Res., Sect. A **368**, 675 (1996).

[44] D. Tománek and M. A. Schluter, Phys. Rev. Lett. **67**, 17 (1991).

[45] V.-V. Elomaa *et al.*, Nucl. Instrum. Methods Phys. Res., Sect. B **266**, 4425 (2008).

[46] V.-V. Elomaa *et al.*, Nucl. Instrum. Methods Phys. Res., Sect. A (submitted) (2009).

[47] M. Aguilar-Benitez *et al.*, Phys. Lett. B **170**, 1 (1986).

[48] V.-V. Elomaa *et al.*, Eur. Phys. J. A **40**, 1 (2009).

[49] V. A. Rubchenya, Phys. Rev. C **75**, 054601 (2007).

[50] A. Kankainen *et al.*, Eur. Phys. J. A **29**, 271 (2006).

[51] H. Penttilä *et al.*, to be submitted (2009).

[52] G. Audi, A. H. Wapstra, and C. Thibault, Nucl. Phys. A **729**, 337 (2003).

[53] V.-V. Elomaa *et al.*, Phys. Rev. Lett. **102**, 252501 (2009).

[54] A. Martín *et al.*, Eur. Phys. J. A **34**, 341 (2007).

[55] P. Möller, J. Nix, and K.-L. Kratz, At. Data Nucl. Data Tables **66**, 131 (1997).

[56] C. Mazzocchi *et al.*, Phys. Rev. Lett. **98**, 212501 (2007).

[57] G. Audi, A. H. Wapstra, and C. Thibault, Nucl. Phys. A **729**, 129 (2003).

[58] A. Plochocki *et al.*, Phys. Lett. B **106**, 285 (1981).

[59] A. Kankainen *et al.*, Phys. Rev. Lett. **101**, 142503 (2008).

[60] I. Mukha *et al.*, Nature **439**, 298 (2006).

[61] D. Kast *et al.*, Z. Phys. A **356**, 363 (1997).

[62] I. Mukha *et al.*, Phys. Rev. Lett. **95**, 022501 (2005).